Point Velocity Measurement

John A. Kleppe
University of Nevada

John G. Olin
Sierra Instruments, Inc.

Rajan K. Menon
TSI Inc.

29.1 Pitot Probe Anemometry

John A. Kleppe

Theory

It is instructive to review briefly the principles of fluid dynamics in order to understand *Pitot tube theory* and applications. Consider, for example, a constant-density fluid flowing steadily without friction through the simple device shown in Figure 29.1. If it is assumed that there is no heat being added and no shaft work being produced by the fluid, a simple expression can be developed to describe this flow:

$$\frac{p_1}{w} + \frac{v_1^2}{2g} + z_1 = \frac{p_2}{w} + \frac{v_2^2}{2g} + z_2 \tag{29.1}$$

where p_1, v_1, z_1 = Pressure, velocity, and elevation at the inlet
p_2, v_2, z_2 = Pressure, velocity, and elevation at the outlet
w = ρg, the specific weight of the fluid
ρ = Density
g = 9.80665 m s^{-2}

Equation 29.1 is the well known Bernoulli equation. The following example will demonstrate the use of Equation 29.1 and lead to a discussion of the theory of Pitot tubes.

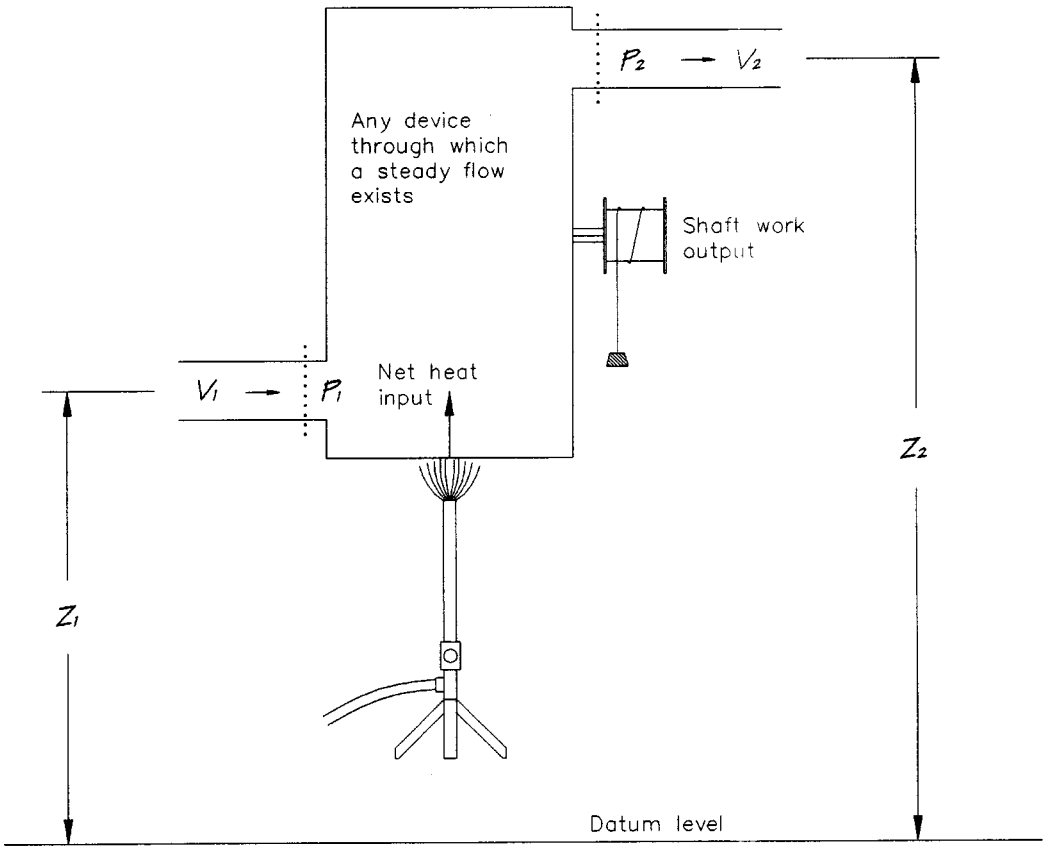

FIGURE 29.1 A device demonstrating Bernoulli's equation for steady flow, neglecting losses. (From [1].)

Example

A manometer [2] is used to measure the dynamic pressure of the tube assembly shown in Figure 29.2 [3]. The manometer fluid is mercury with a density of 13,600 kg m^{-3}. For a measured elevation change, Δh, of 2.5 cm, calculate the flow rate in the tube if the flowing fluids is (a) water, (b) air. Neglect all losses and assume STP conditions for the air flowing in the tube and $g = 9.81$ m s^{-2}.

Solution

Begin by writing expressions for the pressure at point 3.

$$p_3 = h_1\, w_{\mathrm{Hg}} + \left(h_3 - h_1\right) w + p_1 \tag{29.2}$$

and

$$p_3 = h_2\, w_{\mathrm{Hg}} + \left(h_3 - h_2\right) w + p_2 \tag{29.3}$$

Subtracting these equations and rearrangement yields an expression for the pressure difference.

$$p_2 - p_1 = \Delta h \left(w_{\mathrm{Hg}} - w\right) \tag{29.4}$$

where w is the specific weight for water or air, etc.

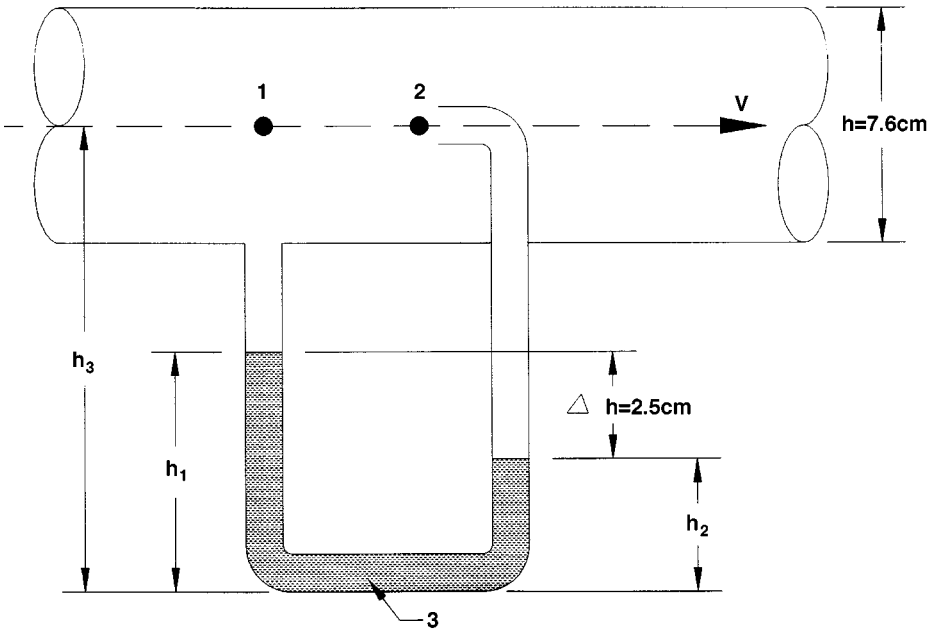

FIGURE 29.2 Using a manometer to measure a Pitot-static tube type assembly - Example (1).

Also using Equation 29.1, one can show that for $z_1 = z_2$ and $v_2 = 0$:

$$p_2 - p_1 = \frac{w\, v_1^2}{2g} \tag{29.5}$$

(a) For water,

$$\begin{aligned} p_2 - p_1 &= \Delta h \left(w_{\mathrm{Hg}} - w_{\mathrm{H_2O}} \right) \\ &= 0.025 \left[13{,}600 \left(9.81 \right) - 998 \left(9.81 \right) \right] \\ &= 3090.6 \text{ Pa} \end{aligned} \tag{29.6}$$

Then,

$$3090.6 = \frac{\left(998 \right)\left(9.81 \right) v_1^2}{2\left(9.81 \right)} \tag{29.7}$$

or

$$v_1 = 2.5 \text{ m s}^{-1} \tag{29.8}$$

The flow Q is then calculated to be:

$$Q = A_1 v_1 = \frac{\pi d^2 v_1}{4} = \frac{\pi\left(.076 \right)^2 \left(2.5 \right)}{4} = 0.011 \text{ m}^3 \text{ s}^{-1} \tag{29.9}$$

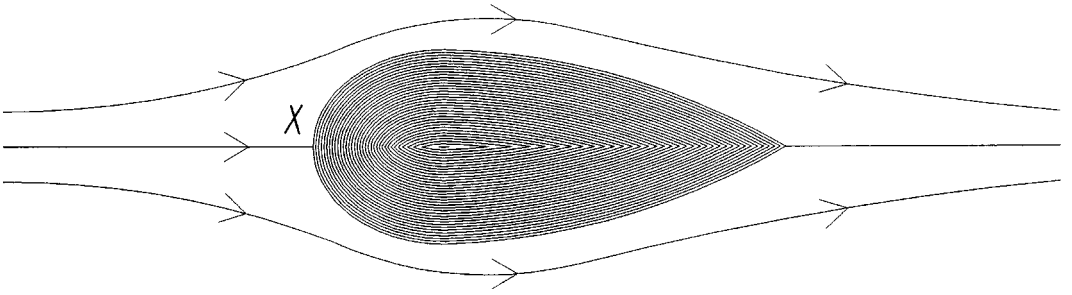

FIGURE 29.3 Flow around a nonrotating solid body.

(b) For air, one can use these same methods to show that:

$$Q = 0.34 \text{ m}^3 \text{ s}^{-1} \tag{29.10}$$

A point in a fluid stream where the velocity is reduced to zero is known as a stagnation point [1]. Any nonrotating object placed in the fluid stream will produce a stagnation point, x, as seen in Figure 29.3. A manometer connected to point x would record the stagnation pressure of the fluid. From Bernoulli's equation (Equation 29.1), the quantity $p + \frac{1}{2}\rho v^2 + \rho gz$ is constant along a streamline for the steady flow of a fluid of constant density. Consequently, if the velocity v at a particular point is brought to zero, the pressure there is increased from p to $p + \frac{1}{2}\rho v^2$. For a constant-density fluid, the quantity $p + \frac{1}{2}\rho v^2$ is known as the stagnation pressure p_0 of that streamline, while the term $\frac{1}{2}\rho v^2$ — that part of the stagnation pressure due to the motion — is termed the dynamic pressure. A manometer connected to point x would measure the stagnation pressure and, if the static pressure p were also known, then $\frac{1}{2}\rho v^2$ could be obtained. One can show that:

$$p_t = p + p_v \tag{29.11}$$

where p_t = Total pressure, which is the sum of the static and dynamic pressures which can be sensed by a probe that is at rest with respect to the system boundaries when it locally stagnates the fluid isentropically

p = The actual pressure of the fluid whether in motion or at rest and can be sensed by a probe that is at rest with respect to the fluid and does not disturb the fluid in any way

p_v = The dynamic or velocity pressure equivalent of the directed kinetic energy of the fluid

Using Equation 29.11, one can develop an expression that relates to the velocity of the fluid:

$$p_t = p + 1/2\rho v^2 \tag{29.12}$$

or, solving for v:

$$v = \sqrt{\frac{2(p_t - p)}{\rho}} \tag{29.13}$$

Consider as an example the tube arrangement shown in Figure 29.4. A right-angled tube, large enough to neglect capillary effects, has one end A facing the flow. When equilibrium is attained, the fluid at A is stationary and the pressure in the tube exceeds that of the surrounding stream by $\frac{1}{2}\rho v^2$. The liquid is forced up the vertical part of the tube to a height:

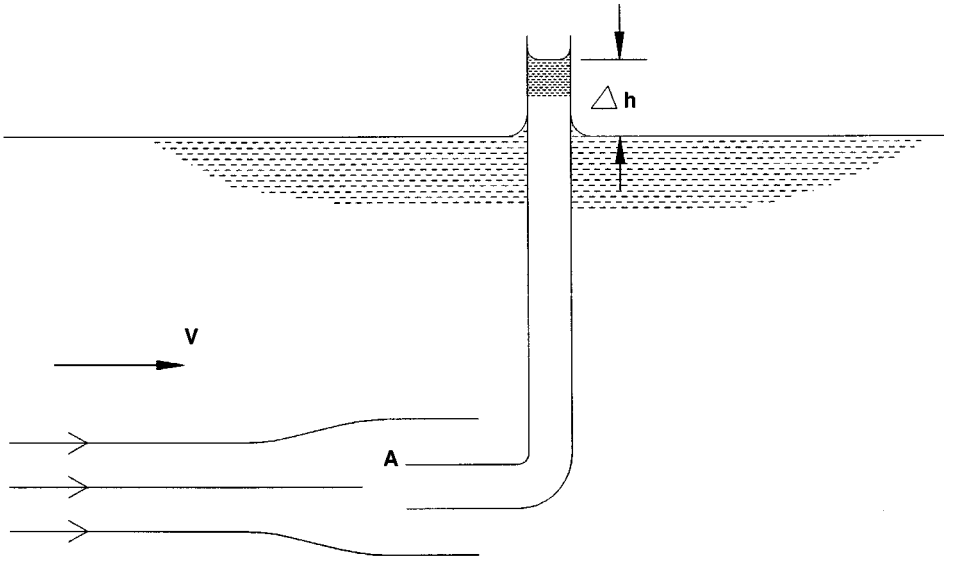

FIGURE 29.4 Right-angle tube in a flow system.

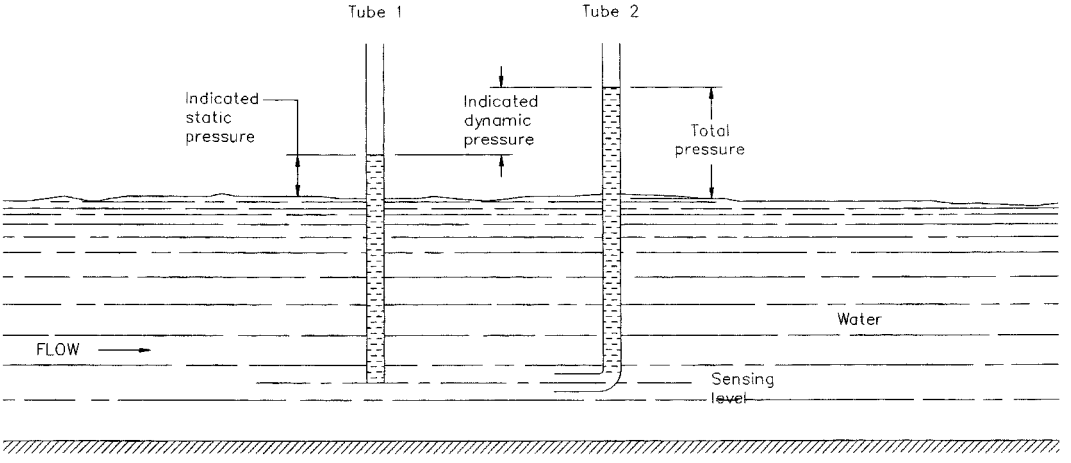

FIGURE 29.5 Basic Pitot tube method of sensing static, dynamic, and total pressure. (From R. P. Benedict, *Fundamentals of Temperature, Pressure and Flow Measurements,* 3rd ed., New York: John Wiley & Sons, 1984. With permission.)

$$\Delta h = \frac{\Delta p}{w} = \frac{v^2}{2g} \tag{29.14}$$

This relationship was used in the example given earlier to solve for *v*. It must be remembered that the total pressure in a fluid can be sensed only by stagnating the flow isentropically; that is, when its entropy is identical at all points in the flow. Such stagnation can be accomplished by a Pitot tube, as first developed by Henri de Pitot in 1732 [4]. In order to obtain a velocity measurement in the River Seine (in France), Pitot made use of two tubes immersed in water. Figure 29.5 shows his basic Pitot tube method. The lower

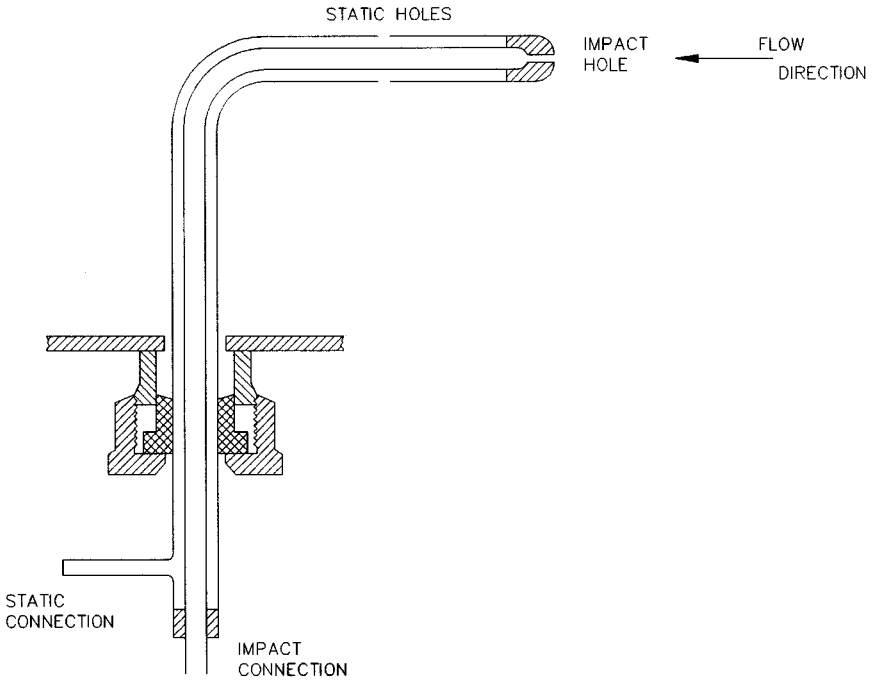

FIGURE 29.6 A modern Pitot-static tube assembly. (From ASME/ANSI PTC 19.2-1987, Instruments and Apparatus, Part 2, Pressure Measurements, 1987. With permission.)

opening in one of the tubes was taken to be a measurement of the static pressure. The rise of fluid in the 90° tube was used as an indication of the velocity of the flow. For reasons to be discussed later, Pitot's method for measuring the static pressure was highly inadequate and would be considered incorrect today [4].

A modern-day Pitot-static tube assembly is shown in Figure 29.6 [5]. The static pressure is measured using "static holes" or pressure taps in the boundary. A pressure tap usually takes the form of a hole drilled in the side of a flow passage and is assumed to sense the "true" static pressure. When the fluid is moving past in the tap, which is usually the case, the tap will not indicate the true static pressure. The streamlines are deflected into the holes as shown in Figure 29.7, setting up a system of eddies. The streamline curvature results in a pressure at the tap "mouth" different from the true fluid pressure. These factors in combination result in a higher pressure at the tap mouth than the true fluid pressure, a positive pressure error. The magnitude of this pressure error is a function of the Reynolds number based on the shear velocity and the tap diameter [5]. Larger tap diameters and high velocities give larger errors [5]. The effect of compressibility on tap errors is not well understood or demonstrated, although correlations for this effect have been suggested [5]. It is possible to reduce tap errors by moving the location of the tap to a nonaccelerating flow location, or use pressure taps of smaller diameter. The effect of edge burrs is also noteworthy. All burrs must be removed. There is also an error that results with the angle of attack of the Pitot tube with the flow direction. Figure 29.8 shows the variation of total pressure indications as a function of the angle of attack. It can be seen that little error results if the angle of attack is less than $\pm 10°$.

A widely used variation of the Pitot-static tube is the type S Pitot tube assembly shown in Figure 29.9. It must be carefully designed and fabricated to ensure it will properly measure the static pressure. The "static" tube faces backwards into the wake behind the probe where the pressure is usually somewhat lower than the undisturbed static pressure. The type S Pitot tube therefore requires the application of a correction factor (usually in the range of 0.84). This correction factor will be valid only over a limited

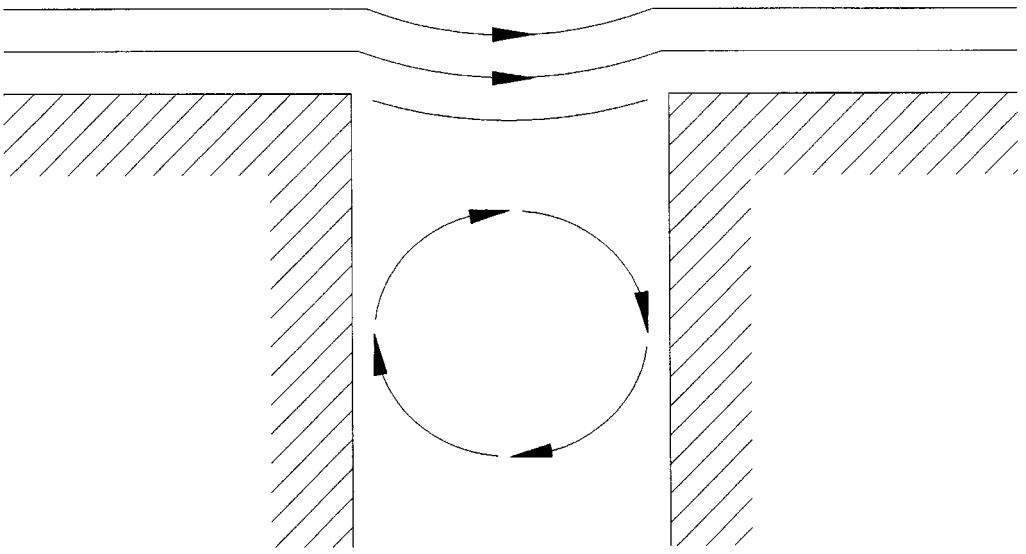

FIGURE 29.7 Pressure tap flow field.

range of velocity measurement. The type S Pitot tube does, however, have the advantage of being compact and relatively inexpensive. A type S Pitot tube can be traversed across a duct or stack to determine the velocity profile and hence total volumetric flow. This is discussed later.

The Pitot Tube in Flow with Variable Density

When a Pitot-static tube is used to determined the velocity of a constant-density fluid, the stagnation pressure and static pressure need not be separately measured: It is sufficient to measure their difference. A high-velocity gas stream, however, can undergo an appreciable change of density in being brought to rest at the front of the Pitot-static tube; under these circumstances, stagnation and static pressures must be separately measured. Moreover, if the flow is initially supersonic, a shock wave is formed ahead of the tube, and, thus, results for supersonic flow differ essentially from those for subsonic flow. Consider first the Pitot-static tube in uniform subsonic flow, as in Figure 29.10.

The process by which the fluid is brought to rest at the nose of the tube is assumed to be frictionless and adiabatic. From the energy equation for a perfect gas, it can be shown that [1]:

$$\frac{v^2}{2} = C_p\left(T_0 - T\right) = C_p T_0 \left\{1 - \left(\frac{p}{p_0}\right)^{(\gamma-1)/\gamma}\right\} \tag{29.15}$$

where v = Velocity
C_p = Specific heat at constant pressure
T = Absolute temperature of the gas
T_0 = Absolute temperature at stagnation conditions
p = Total pressure
γ = Ratio of specific heats

For measuring T_0, it is usual to incorporate in the instrument a small thermocouple surrounded by an open-ended jacket. If T_0 and the ratio of static to stagnation pressure are known, the velocity of the stream can then be determined from Equation 29.15.

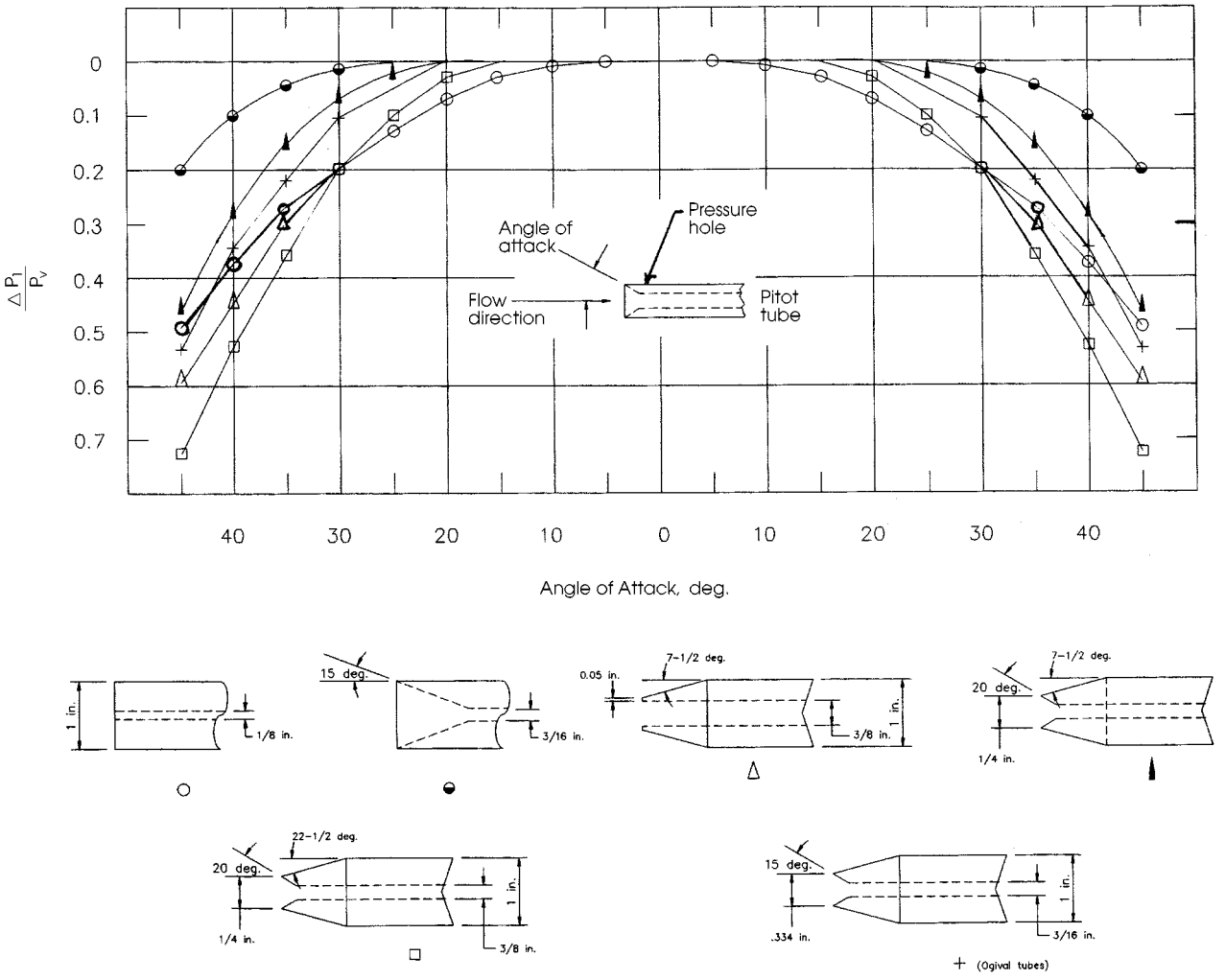

FIGURE 29.8 Variation of total pressure indication with angle of attach and geometry for Pitot tubes. (From ASME/ANSI PTC 19.2-1987, Instruments and Apparatus, Part 2, Pressure Measurements, 1987. With permission.)

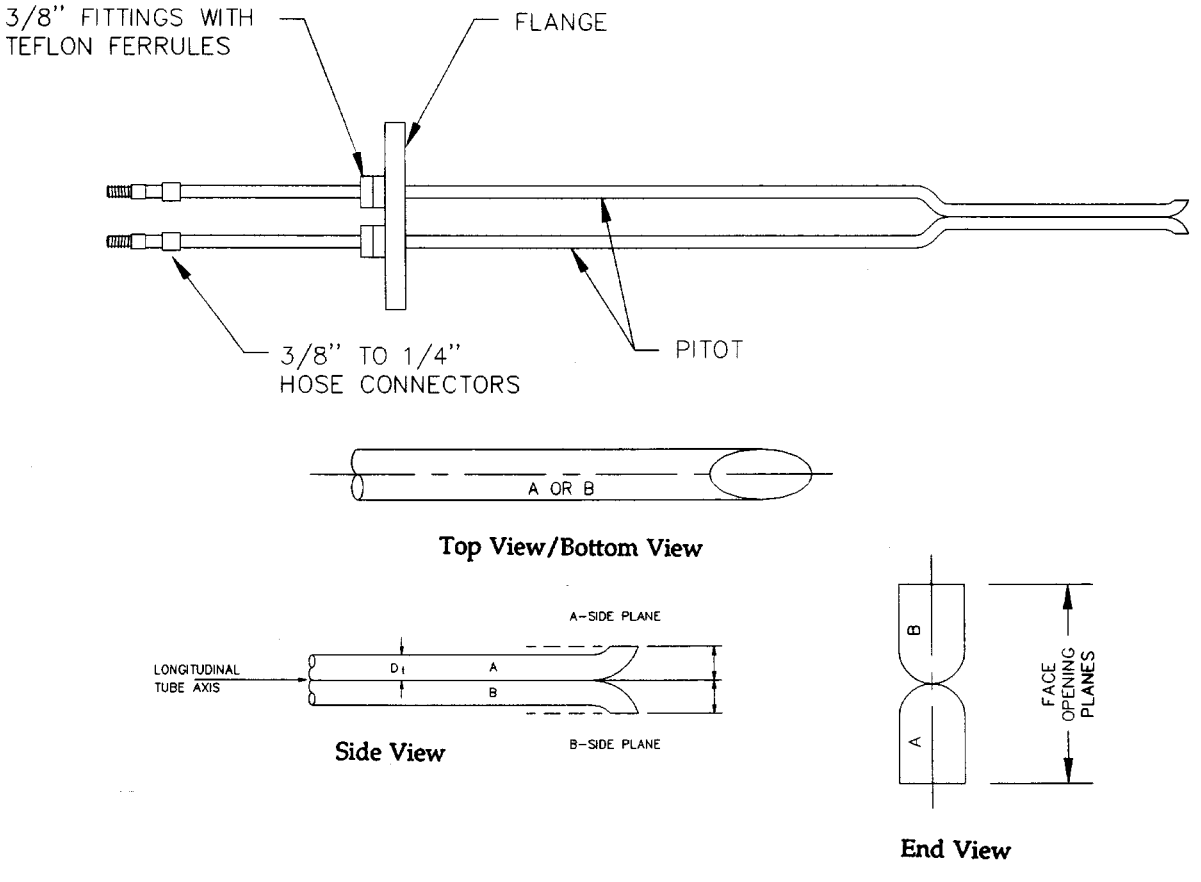

FIGURE 29.9 An S type Pitot tube for use in gas flow measurement will have specific design parameters. For example, the diameter of the tubing D_t, a gas probe will be between 0.48 and 0.95 cm. There should be equal distances from the base of each leg of the Pitot tube to its face opening plane, dimensions d_1, d_2. This distance should be between 1.05 and 1.50 times the external tubing diameter, D_t. The face openings of the Pitot tube should be aligned as shown. This configuration of the type S Pitot tube results in a correction coefficient of approximately 0.84. (From EPA, CFR 40 Part 60, Appendix A—Test Methods, 1 July 1995.)

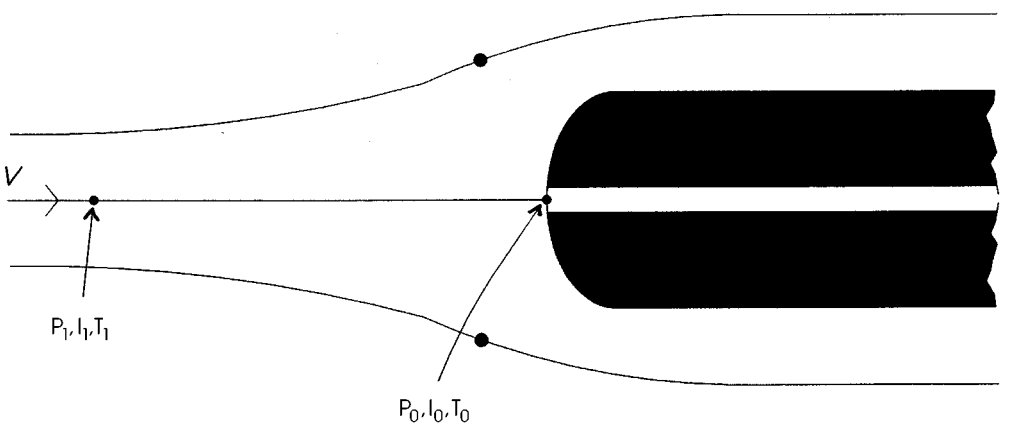

FIGURE 29.10

The influence of compressibility is best illustrated using the Mach number, *M*. It can be shown that: [1]

$$\frac{p_0}{p} = \left(1 + \frac{\gamma - 1}{2} M^2\right)^{\gamma/(\gamma-1)} \tag{29.16}$$

For subsonic flow, $[(\gamma - 1)/2]M^2 < 1$ and so the right side of Equation 29.16 can be expanded by the binomial theorem to give:

$$\frac{p_0}{p} = 1 + \frac{\gamma}{2} M^2 + \frac{\gamma}{8} M^4 + \frac{\gamma(2-\gamma)}{48} M^6 + \ldots \tag{29.17}$$

$$p_0 - p = \frac{p\gamma M^2}{2}\left\{1 + \frac{M^2}{4} + \left(\frac{2-\gamma}{24}\right) M^4 + \ldots\right\} \tag{29.18}$$

$$= 1/2\ \rho v^2 \left\{1 + \frac{M^2}{4} + \left(\frac{2-\gamma}{24}\right) M^4 + \ldots\right\} \tag{29.19}$$

The bracketed quantity is the compressibility factor and represents the effect of compressibility. Table 29.1 indicates the variation of the compressibility factor with *M* for air with $\gamma = 1.4$

It is seen that for $M < 0.2$, compressibility affects the pressure difference by less than 1%, and the simple formula for flow at constant density is then sufficiently accurate. For larger values of *M*, however, the compressibility must be taken into account.

For supersonic flow, Equation 29.16 is not valid because a shock wave forms ahead of the Pitot tube, as shown in Figure 29.11 and, thus, the fluid is not brought to rest isentropically. The nose of the tube must be shaped so that the shock wave is detached, i.e., the semiangle must be greater than 45.6° [1].

If the axis of the tube is parallel to the oncoming flow, the wave can be assumed normal to the streamline leading to the stagnation point. The pressure rise across the shock can therefore be given by:

$$\frac{p_2}{p_1} = \frac{1 + \gamma M_1^2}{1 + \gamma M_2^2} \tag{29.20}$$

TABLE 29.1 Variation of "Compressibility Factor" for Air

M	$\frac{P_0 - P}{\frac{1}{2}\rho v^2}$
0.1	1.003
0.2	1.010
0.3	1.023
0.4	1.041
0.5	1.064
0.6	1.093
0.7	1.129
0.8	1.170
0.9	1.219
1.0	1.276

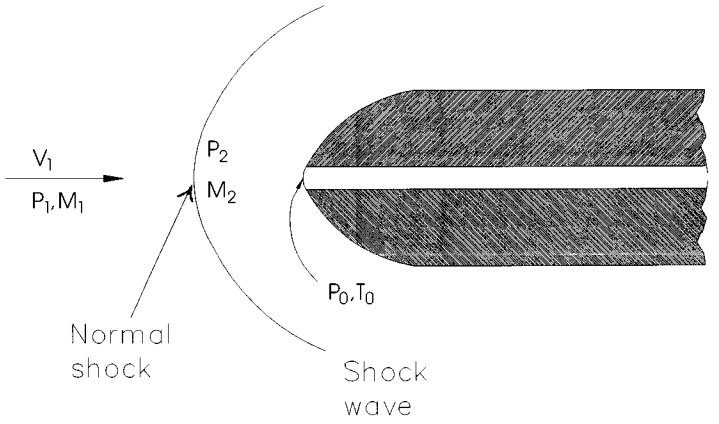

FIGURE 29.11

In the subsonic region downstream of the shock, there is a gradual isentropic pressure rise that can be represented as:

$$\frac{p_0}{p_1} = \frac{p_0}{p_2}\frac{p_2}{p_1} = \left(1 + \frac{\gamma - 1}{2} M_2^2\right)^{\gamma/(\gamma-1)} \frac{1 + \gamma M_1^2}{1 + \gamma M_2^2} \tag{29.21}$$

Finally, one obtains Rayleigh's formula:

$$\frac{p_0}{p_1} = \left\{ \frac{(\gamma+1)^{\gamma+1}}{2\gamma M_1^2 - \gamma + 1} \left(\frac{M_1^2}{2}\right)^{\gamma} \right\}^{1/(\gamma-1)} \tag{29.22}$$

This expression for air reduces to:

$$\frac{p_0}{p_1} = \frac{166.9 M_1^7}{\left(7M_1^2 - 1\right)^{2.5}} \quad \text{when } \gamma = 1.4 \tag{29.23}$$

Although a conventional Pitot-static tube gives satisfactory results at Mach numbers low enough for no shock waves to form, it is unsuitable in supersonic flow because its "static holes" or "pressure taps", being in the region downstream of the shock, do not then register p_1; nor do they register p_2 since this is found only on the central streamline, immediately behind the normal part of the shock wave. Consequently, p_1 is best determined independently — for example, through an orifice in a boundary wall well upstream of the shock. Where independent measurement of p_1 is not possible, a special Pitot-static tube can be used, in which the static holes are much further back (about 10 times the outside diameter of the tube) from the nose. The oblique shock wave on each side of the tube has by then degenerated into a Mach wave across which the pressure rise is very small.

When $M_1 = 1$, the pressure rise across the shock is infinitesimal and, thus, Equations 29.16 and 29.22 both give:

$$\frac{p_0}{p_1} = \left\{\left(\gamma+1\right)/2\right\}^{\gamma/\left(\gamma-1\right)} = 1.893 \left(\text{for air}\right) \tag{29.24}$$

A small value of p_0/p therefore indicates subsonic flow, a larger value supersonic flow.

Notice that Equation 29.22 enables the upstream Mach number to be calculated from the ratio of stagnation to static pressure. Since the stagnation temperature does not change across a shock wave:

$$C_p T_0 = C_p T_1 + \frac{v_1^2}{2} = C_p \frac{v_1^2}{\gamma R M_1^2} + \frac{v_1^2}{2} \tag{29.25}$$

Thus, v_1 can also be calculated if T_0 is determined.

Volumetric Flow Measurements

The currently accepted method for measuring volumetric gas flow in ducts and stacks involves the use of Pitot tubes to obtain the velocity at points of equal area of the cross-sectional areas of the stack [7]. For example, Figure 29.12 shows a case where the circular stack of cross-sectional area A has been divided into twelve (12) equal areas. An estimate of the average volumetric flow velocity is determined using the following relationship:

$$\bar{v}_n \approx \frac{\Sigma\, v_n A_n}{A} = \frac{A_i \,\Sigma\, v_n}{N A_i} = \frac{1}{N} \Sigma\, v_n \tag{29.26}$$

where A_i = One segment of the equal area segments
N = Number of equal area segments
v_n = Velocity measured at each point of equal area segment

This relationship shows that one can estimate the average volumetric flow velocity by taking velocity measurements at each point of equal area and then calculate the arithmetic mean of these measurements. It is clearly seen that a different result would be obtained if one were to simply take velocity measurements at equidistant points across the measurement plane and then take the arithmetic mean of these measurements. What would result in this case would be the path-averaged velocity, $\bar{v}_p$, which would be in error.

The sampling site and the number of traverse points designated will affect the quality of the volumetric flow measurement. The acceptability of the sampling procedure is generally determined by the distances from the nearest upstream and downstream disturbances (obstruction or change in direction) to gas flow. The minimum requirements for an acceptable sampling procedure can be found in the literature [7].

An automated system for accomplishing this measurement is shown in Figure 29.13 [8].

Traverse point	Distance % of diameter
1	4.4
2	14.6
3	29.6
4	70.4
5	85.4
6	95.6

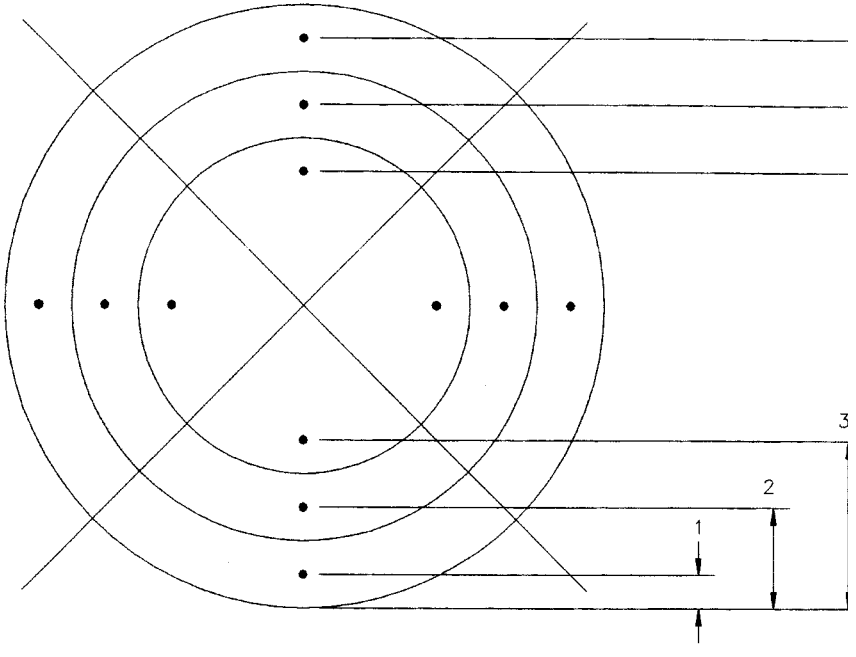

FIGURE 29.12 Example showing circular stack cross-section divided into 12 equal areas, with location of traverse points indicated.

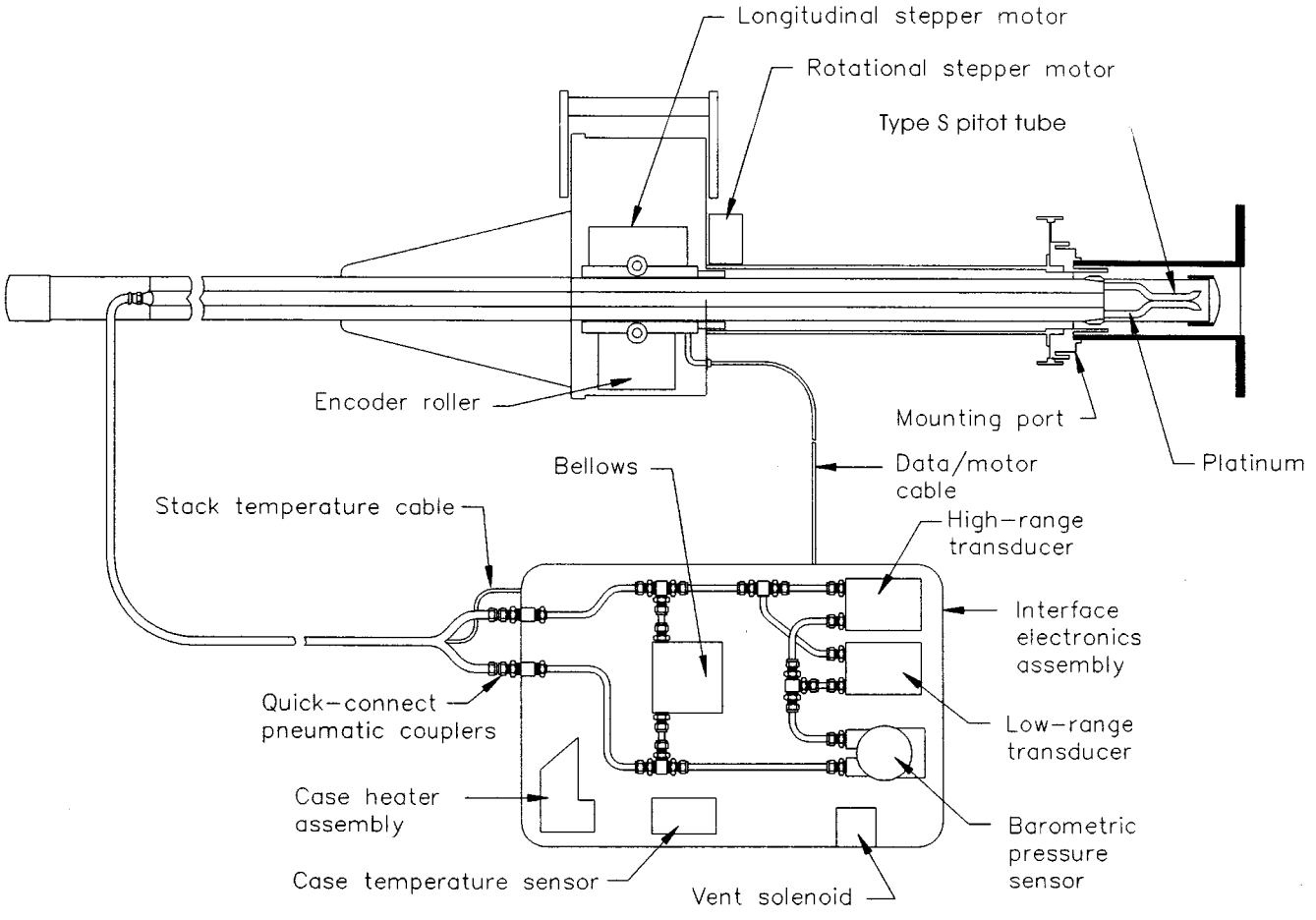

FIGURE 29.13 Automated probe consists of a type S Pitot tube and a platinum RTD mounted onto a type 319 stainless steel probe. (From T. C. Elliott, CEM System: Lynchpin Holding CAA Compliance Together, *Power,* May 1995, 31–40. With permission.)

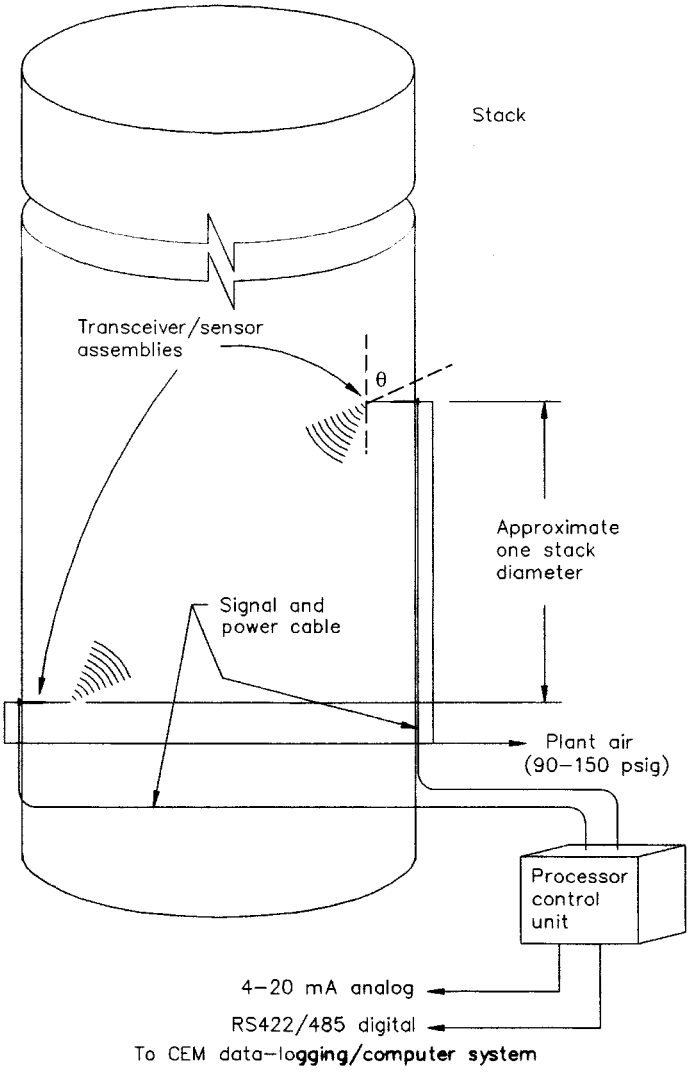

FIGURE 29.14 Block diagram of the hybrid system.

A Hybrid System

A hybrid system that combines sonic (acoustic) and Pitot tube technology has been developed to measure volumetric flow in large ducts and stacks [9–12]. A block diagram of this system is shown in Figure 29.14. The sensors (Figure 29.15) are mounted on opposite sides of the stack or duct at an angle θ to the flow direction. The acoustic portion of the sensor measures the flight time of the sound waves with and against the gas flow. It can easily be shown [9] that by transmitting and receiving the sound waves in opposite directions, the path average velocity of the gaseous medium can be determined from:

$$\bar{v}_p = \frac{d}{2\cos\theta}\left(\frac{\tau_2 - \tau_1}{\tau_1\,\tau_2}\right) \text{m s}^{-1} \tag{29.27}$$

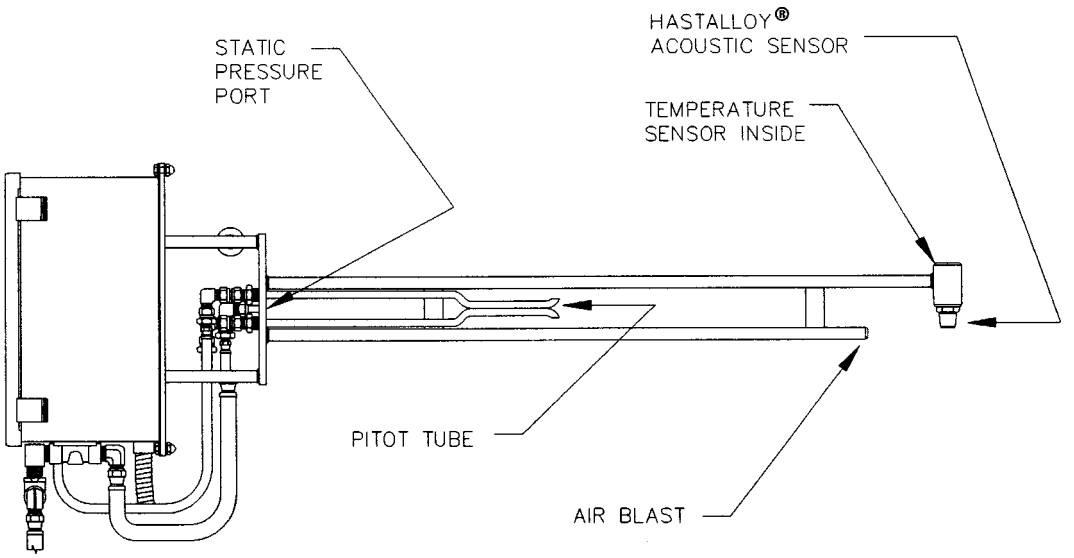

FIGURE 29.15 Acoustic probe contains acoustic, Pitot, and temperature sensors.

where $\bar{v}_p$ = Path average velocity of the gas m s^{-1}
d = Distance between the transceivers (m)
θ = Angle, in degrees, of the path of the transducers with the vertical
τ_1 = Flight time of the sound with the gas flow (s)
τ_2 = Flight time of the sound against gas flow (s)

The result of this part of the total measurement is the area under the velocity curve plotted in Figure 29.16. The Pitot tubes provide differential pressure measurements at two points within the stack. The differential pressure is converted to velocity in a unique manner. The flight times of the acoustic wave, when properly combined with the temperature sensor reading, provide a measurement of the molecular weight of the wet flue gas. This value is then used to obtain the point velocity measurements shown as V_2 and V_3 in Figure 29.16. The actual flow profile curve is then estimated using the values V_1, V_2, V_3, and V_4 and the area under the flow profile curve generated by the acoustic portion of the system. The final part of the measurement involves using the static pressure measurements and the stack temperature measurements to calculate the total standard volumetric flow in scfh (wet).

Commercial Availability

There are a variety of material used to construct Pitot tubes. The reasons for this are that Pitot tubes are used to measure a wide range of fluids. For example, to use a type S Pitot tube in a large power plant stack with a wet scrubber where the environment is extremely hostile and corrosive, stainless steel 316 or C276 (Hastaloy®) must be used. This, of course, makes the price of the Pitot tube as varied as its application. Many of the basic type S Pitot tube probes themselves are manufactured by a few small companies who, in turn, supply them on an OEM basis to others.

A typical type S Pitot tube assembly, such as that shown in Figure 29.9, constructed using stainless steel 316 can be purchased (in small quantities) for $310 each. They are available from:

EEMC/EMRC
3730 North Pellegrino Drive
Tucson, AZ 85749
Tel: (520) 749-2167
Fax: (520) 749-3582

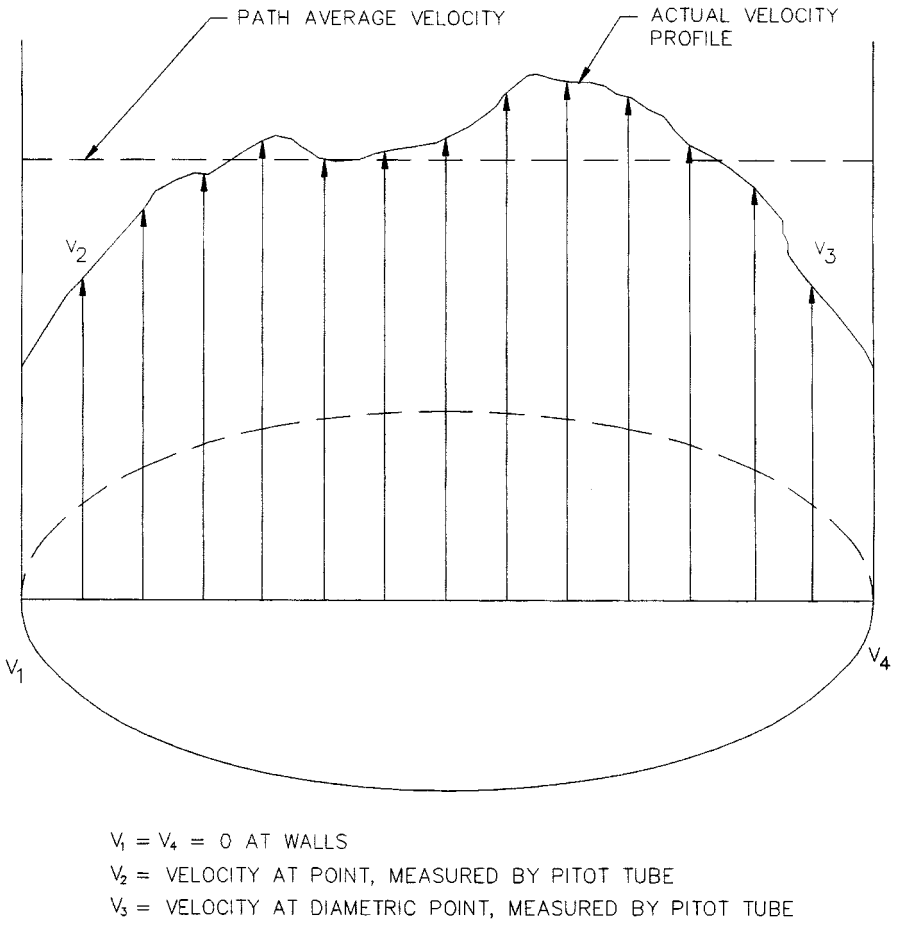

FIGURE 29.16 The velocity profile in a typical large duct or stack can vary greatly, thus changing the total volumetric flow. The hybrid system assumes V_1 and V_4 to be zero; measures V_2 and V_3 using the Pitot tubes; and provides the path average (area under the curve) using the acoustic portions of this sensor.

A typical modern Pitot-static assembly, such as that shown in Figure 29.6, can be purchased (in small quantities) for $34 and are available from:

Dwyer Instruments, Inc.
P.O. Box 373
Michigan City, IN 46361
Tel: (219) 879-8000
Fax: (219) 872-9057

More complex, custom-designed and fabricated Pitot-static probes for use on aircraft are available from:

Rosemount Aerospace Inc.
14300 Judicial Road
Burnsville, MN 55306-4898
Tel: (612) 892-4300
Fax: (612) 892-4430

Table 29.2 lists a number of manufactures/vendors that sell Pitot tube and general differential pressure measurement instrumentation.

TABLE 29.2 A Sample of Manufacturers/Vendors

Name	Address	Telephone/Fax	Probe Type
EEMC/EMRC	3730 North Pellegrino Dr. Tucson, AZ 85749	Tel: (520) 749-2167 Fax: (520) 749-3582	Type S Pitot probe
Dwyer Instruments, Inc.	P.O. Box 373 Michigan City, IN 46361	Tel: (219) 879-8000 Fax: (219) 872-9057	Pitot-static tubes and type S Pitot probe
Rosemount Aerospace, Inc.	14300 Judicial Rd. Burnsville, MN 55306-4898	Tel: (612) 892-4300 Fax: (612) 892-4430	Flow angle sensors, Pitot/Pitot-static tubes, vane angle of attack sensors, temperature sensors, ice detectors, and pressure transducers
Dieterich Standard	P.O. Box 9000 Boulder, CO 80301	Tel: (303) 530-9600 Fax: (303) 530-7064	Multipoint, self-averaging ANNUBAR®
Air Monitor Corporation	P.O. Box 6358 Santa Rosa, CA 95406	Tel: (707) 544-2706 (800) AIRFLOW Fax: (707) 526-9970	Multipoint, self-averaging
United Sciences, Inc.	5310 North Pioneer Rd. Gibsonia, PA 15044	Tel: (412) 443-8610 Fax: (412) 443-7180	Auto-PROBE 2000® automated Method 2 Testing
Scientific Engineering Instruments, Inc.	1275 Kleppe Lane, Suite 14 Sparks, NV 89431-6499	Tel: (702) 358-0937 Fax: (702) 358-0956	STACKWATCH® Hybrid System for volumetric flow sensing in large ducts and stacks (CEMS)

References

1. B. S. Massey, *Mechanics of Fluids,* Princeton, NJ: Van Nostrand, 1968.
2. W. F. Hughes and J. A. Brighton, *Theory and Problems of Fluid Dynamics,* New York: McGraw-Hill, 1967.
3. J. B. Evett and C. Liu, *Fluid Mechanics and Hydraulics: 2500 Solved Problems,* New York: McGraw-Hill, 1989.
4. R. P. Benedict, *Fundamentals of Temperature, Pressure and Flow Measurements,* 3rd ed., New York: John Wiley & Sons, 1984.
5. ASME/ANSI PTC 19.2 - 1987, *Instruments and Apparatus, Part 2, Pressure Measurement,* 1987.
6. S. P. Parker, *Fluid Mechanics Source Book,* New York: McGraw-Hill, 1988.
7. EPA, *CFR 40 Part 60, Appendix A—Test Methods,* 1 July 1995.
8. T. C. Elliott, CEM System: Lynchpin Holding CAA Compliance Together, *Power,* May 1995, 31–40.
9. J. A. Kleppe, Principles and Applications of Acoustic Sensors Used for Gas Temperature and Flow Measurement, *Proc. SENSOR EXPO,* Boston, May 1995, 337–374.
10. J. A. Kleppe, Acoustic Gas Flow Measurement in Large Ducts and Stacks, *Sensors J.,* 12(5), 18–24 and 85–87, 1995.
11. *Guidelines for Flue Gas Flow Rate Monitoring,* EPRI TR-104527, Project 1961-13 Final Report, June 1995.
12. A. Mann and J. A. Kleppe, A Report on the Performance of a Hybrid Flow Monitor Used for CEMS and Heat Rate Applications, *Proc. EPRI 1996 Heat Rate Improvement Conf.,* Dallas, TX, May 1996, Part 33, 1–13.

29.2 Thermal Anemometry

John G. Olin

General Description

A thermal anemometer measures the velocity at a point in a flowing fluid — a liquid or a gas. Figure 29.17 shows a typical industrial thermal anemometer used to monitor velocity in gas flows. It has two sensors — a velocity sensor and a temperature sensor — that automatically correct for changes in gas temperature.

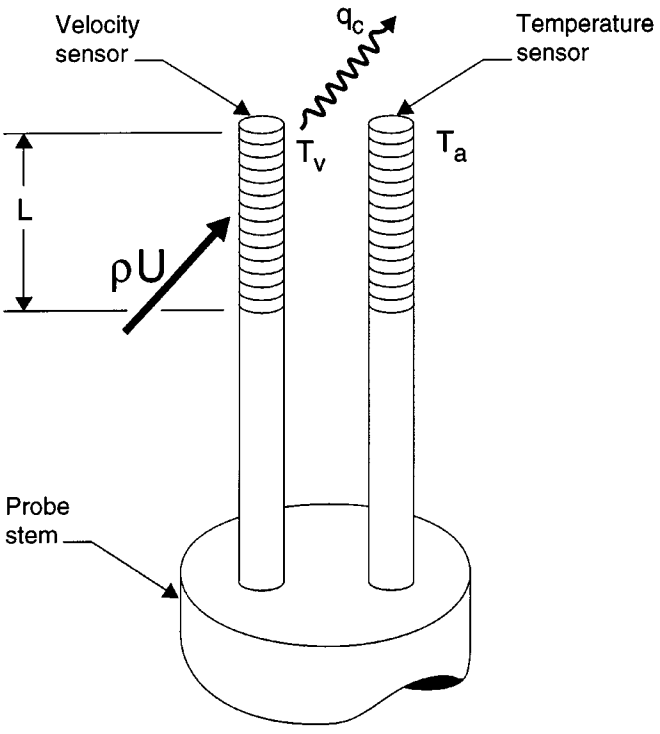

FIGURE 29.17 The principle of operation of a typical industrial thermal anemometer. T_v is the temperature of the heated velocity sensor; T_a is the gas temperature measured by the temperature sensor; ρ is the gas mass density; U is the gas velocity; q_c is the heat carried away by the flowing gas stream; and L is the length of the heated tip of the sensor. (Reprinted with the permission of Sierra Instruments, Inc.)

Both sensors are reference-grade platinum resistance temperature detectors (RTDs). The electric resistance of RTDs increases as temperature increases. For this reason, they are one of the most commonly used sensors for accurate temperature measurements. The electronics circuit passes current through the velocity sensor, thereby heating it to a constant temperature differential ($T_v - T_a$) above the gas temperature T_a and measures the heat q_c carried away by the cooler gas as it flows past the sensor. Hence, it is called a "constant-temperature thermal anemometer."

Because the heat is carried away by the gas molecules, the heated sensor directly measures gas mass velocity (mass flow rate per unit area) ρU. The mass velocity is typically expressed as U_s in engineering units of normal meters per second, or *normal* m s^{-1}, referenced to normal conditions of 0°C or 20°C temperature and 1 atm pressure. If the fluid's temperature and pressure are constant, then the anemometer's measurement can be expressed as *actual* meters per second, or m s^{-1}. When the mass velocity is multiplied by the cross-sectional area of a flow channel, the mass flow rate through the channel is obtained. Mass flow rate, rather than volumetric flow rate, is the direct quantity of interest in most practical and industrial applications, such as any chemical reaction, combustion, heating, cooling, drying, mixing, fluid power, human respiration, meteorology, and natural convection.

The thermal anemometer is often called an *immersible* thermal mass flowmeter because it is immersed in the flow stream, in contrast to the *capillary-tube* thermal mass flowmeter, another thermal methodology commonly configured as an in-line mass flowmeter for low gas flows. The thermal anemometer has some advantages and disadvantages when compared with the two other common point-velocity instruments — Pitot tubes and laser Doppler anemometers. Compared with Pitot tubes, the thermal anemometer measures lower velocities, has much wider rangeability, and can be made smaller, but it generally has a higher cost and is not recommended for nonresearch liquid flows. When thermal anemometers are

compared with laser Doppler anemometers, they have a much lower cost, do not require seeding the flow with particles, can have a faster time response, can be made to have better spatial resolution, and can have a higher signal-to-noise ratio. On the other hand, in nonfluctuating flows, laser Doppler anemometers provide a fundamental measurement of velocity, independent of temperature and fluid properties. For this reason, they are often used to calibrate thermal anemometers.

Thermal anemometers are subdivided into two categories: industrial and research. Figure 29.18 shows typical sensors of industrial and research thermal anemometers.

Industrial Thermal Anemometers

Industrial thermal anemometers measure the point velocity or point mass velocity of gases in most practical and industrial applications. They seldom are used to monitor liquid flows because avoidance of cavitation problems limits the temperature T_v of the velocity sensor to only 10°C to 20°C above the liquid temperature, resulting in reduced velocity sensitivity and increased dependence on small changes in liquid temperature. Additionally, industrial liquid flows can cause sensor contamination and fouling. Typical gases monitored by industrial thermal anemometers include air, nitrogen, oxygen, carbon dioxide, methane, natural gas, propane, hydrogen, argon, helium, and stack gases. Common applications are: combustion air; preheated air; fuel gas; stack gas; natural gas distribution; semiconductor manufacturing gas distribution; heating, ventilation, and air conditioning; multipoint traversals of large ducts and stacks; drying; aeration and digester gas; occupational safety and health monitoring; environmental, natural convection, and solar studies; fermentors; and human inhalation monitoring. Industrial thermal anemometers have become the most commonly used instrument for monitoring the point velocity of gases.

The velocity sensor of an industrial thermal anemometer is a reference-grade platinum wire (approximately 25 μm in diameter and 20 Ω in resistance) wound around a cylindrical ceramic mandrel, such as alumina. Alternatively, the sensor is a thin platinum film deposited on a glass or ceramic substrate. To withstand the harsh environment encountered in many industrial applications, the cylindrical platinum RTD is tightly cemented into the tip of a thin-walled, stainless-steel, Hastelloy, or Inconel tube (typically 3 mm outside diameter and 2 cm to 6 cm long). Because the gas temperature usually varies in industrial applications, industrial thermal anemometer probes almost always have a separate, but integrally mounted, unheated platinum RTD sensor for measuring the local gas temperature T_a. When operated in the constant-temperature anemometer mode, the temperature difference $(T_v - T_a)$ is usually in the 30°C to 100°C range. The temperature sensor is constructed just like the velocity sensor, but has a resistance in the 300 Ω to 1000 Ω range. As shown in Figure 29.17, the dual-sensor probe has the velocity and temperature sensor mounted side-by-side on a cylindrical probe stem (usually 6 mm to 25 mm in diameter and 0.1 m to 3 m long). A shield usually is provided to prevent breakage of the sensing head. The spatial resolution of this industrial thermal anemometer is 1 cm to 2 cm. The electronics for the industrial thermal anemometer is usually mounted directly on the probe stem in an explosion-proof housing. Industrial thermal anemometer systems like this measure gas velocity over the range of 0.5 normal m s^{-1} to 150 normal m s^{-1}.

In use, the industrial thermal anemometer probe is inserted through a sealed compression fitting or flanged stub in the wall of a duct, pipe, stack, or other flow passage. In this case, it is usually called an *insertion* thermal mass flowmeter. In another common configuration, the dual-sensor probe is permanently fitted into a pipe or tube (typically 8 mm to 300 mm in diameter) with either threaded or flanged gas connections. This configuration is called an *in-line* thermal mass flowmeter. In-line meters are directly calibrated for the total gas mass flow rate flowing through the pipe. The several flow body sizes facilitate mass flow monitoring over the range of 10 mg s^{-1} to 10 kg s^{-1}.

Research Thermal Anemometers

Research thermal anemometers measure the point velocity and/or turbulence of clean gases and liquids in research, product development, and laboratory applications. Because of their more fragile nature, they are not used for industrial applications. Typically, the gas is ambient air. Constant-temperature, filtered, degasified water is the primary liquid application, but the technique has also been applied to clean

INDUSTRIAL THERMAL SENSORS

Dual Sensor, Sheathed

Sensors: Dual platinum windings in stainless steel sheaths.

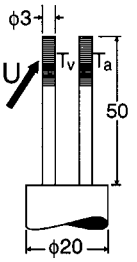

Micro-Machined or Thin-Film Sensor

Sensors: Two microelectronics RTDs in silicon wafer or thin-film platinum RTDs on alumina chip.

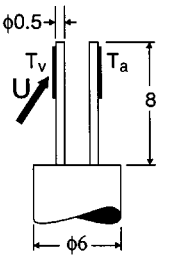

Dual Sensor, Unsheathed

Sensors: Dual platinum windings, glass coated.

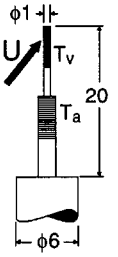

Multi-Point Flow Averaging Array

Sensors: 2 or 4 multi-point probes with 1 to 4 dual sheathed sensors each located at the centroid of equal areas in duct's cross-section.

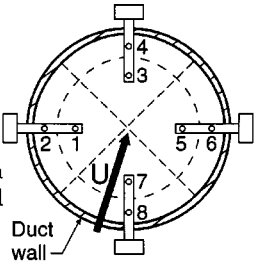

RESEARCH THERMAL SENSORS

Single Normal Hot-Wire Probe

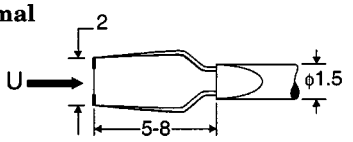

Sensor: Single 5 μm diameter tungsten wire, plated at ends.

***"X"* Hot-Wire Probe**

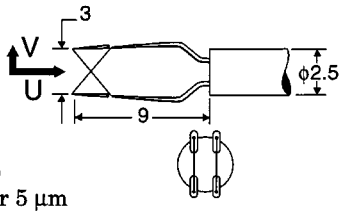

Sensors: Two perpendicular 5 μm diameter tungsten hot wires.

Single Hot-Film Probe

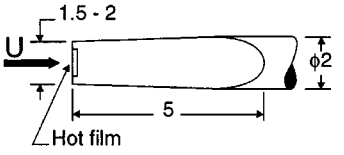

Sensor: Single quartz coated platinum film 0.1 μm thick x 0.1 mm width x 1 mm length, both sides.

3-D Hot-Wire Probe

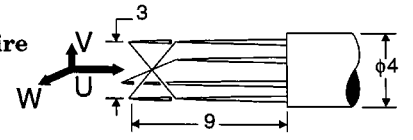

Sensors: Three orthogonal 5 μm diameter tungsten hot wires.

FIGURE 29.18 Typical industrial and research thermal anemometer sensors. All dimensions are in millimeters. T_v indicates the heated velocity sensor; T_a indicates the temperature sensor; U is the major velocity component in the x-direction; V is the transverse velocity component in the y-direction; and W is the transverse velocity component in the z-direction.

hydrocarbon liquids. As shown in Figure 29.18, the research anemometer's velocity sensor is either a hot wire or a hot film. Hot-wire sensors have a high frequency response and, therefore, are excellent for turbulence measurements in air and other gases. They are seldom used in liquid flows because they are susceptible to fouling and contamination. Hot-film sensors trade off lower frequency response for increased ruggedness and are used in gas and liquid flows. For liquid flows, hot-film sensors are designed to shed lint and other fouling or contaminating materials. Bruun [1] is an excellent reference source for the theory and applications of hot-wire and hot-film anemometers. Another comprehensive source is Fingerson and Freymuth [2].

Typical applications for hot-wire and hot-film anemometers include: one-, two-, and three-dimensional flow and turbulence studies; validation of computational fluid dynamics codes; environmental and micrometeorological measurements; turbomachinery; internal combustion engines; biological studies; heat-transfer research; boundary-layer measurements; supersonic flows; two-phase flows; and vorticity measurements. Freymuth [3] describes the 80-year history of research thermal anemometers. Today, hot-wire and hot-film anemometers have become the most widely used instruments for fluid mechanics research and development studies.

The typical hot-wire sensor is a fine tungsten wire welded at each end to miniature prongs designed to minimize their influence on the wire's flow field. The wire is usually gold or copper plated a short length at each end to define an active sensor length away from the two prongs. For work in water, the wire is quartz coated to prevent electrolysis or electrical shorting, but, in this case, cracking of the coating can occur. A typical tungsten wire has a diameter of 4 μm to 5 μm, an active length of 1 mm to 3 mm, and an electrical resistance of 2 Ω to 6 Ω. Because it oxidizes above 350°C in air, tungsten hot wires are usually operated at a temperature not exceeding 300°C. Platinum, 90% platinum + 10% rhodium, and 80% platinum + 20% iridium wires also are used. They can be soldered onto the prongs, but are weaker than tungsten. In cases where the fluid temperature T_a changes enough to cause measurement errors, a separate sensor is used to measure T_a and make temperature corrections. The temperature sensor is either a hot wire or a larger wire-wound RTD mounted either on a separate probe or integrally on the same probe stem as the velocity sensor. As shown in Figure 29.18, for two-dimensional or three-dimensional flow studies, probes with two perpendicular wires in an "X" pattern or three orthogonal wires are used, respectively. Special subminiature probes and probes with the prongs displaced from the probe stem are used for near-wall, boundary-layer work and small flow passages. Gibbings et al. [4, 5] describe hot-wire probes for use in near-wall, turbulent boundary-layer studies.

As shown in Figure 29.18, the typical hot-film sensor is a wedge-tipped or cone-tipped quartz rod with a thin 0.1 μm thick platinum film plated on its tip via cathode sputtering. The platinum film usually is coated with a 1 μm to 2 μm layer of quartz for protection and to avoid electrical shorting or electrolysis in water flows. Because hot-film sensors have a much larger mass than hot-wire sensors, their frequency response is not as flat as hot wires; hence, they are not quite as good for high frequency turbulence measurements. It also has been observed by Mikulla [6] that the shape of some hot-film sensors can suppress response to the turbulent velocity component normal to its surface. On the other hand, hot-film sensors have less breakage and a more stable geometry than hot-wire sensors. Other configurations of hot-film sensors include cylindrical quartz rods (approximately 25 μm to 150 μm in diameter); one or more split-film cylindrical sensors for multidimensional measurements; and flush-mounted sensors for wall heat-transfer measurements.

Principle of Operation

First Law of Thermodynamics

Figure 29.19 shows the first law of thermodynamics applied to a control volume consisting of the velocity sensor of either an industrial thermal anemometer, such as shown in Figure 29.17, or a research thermal anemometer. Application of the first law to thermal anemometer sensors provides the basis for determining point velocity. Applied to Figure 29.19, the first law states that the energy into the control volume

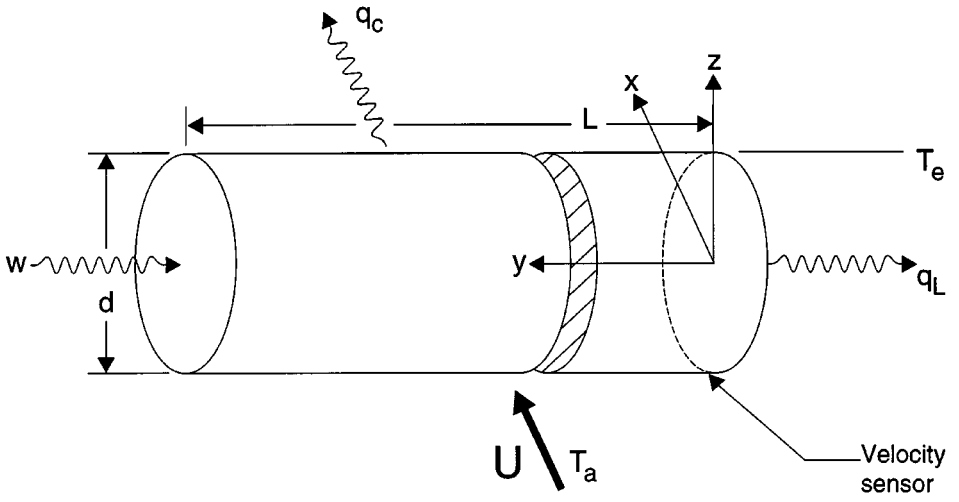

FIGURE 29.19 First law of thermodynamics applied to a thermal anemometer velocity sensor. The term w is the electric power (Watts) supplied to the sensor; q_c is the heat convected away from the sensor by the flowing fluid having a velocity U and temperature T_a; q_L is the conductive heat lost; T_e is the average surface temperature of the sensor over its length L; and d is the sensor's outside diameter.

equals the energy out plus the energy stored. Making the practical simplifying assumptions of steady-state operation (i.e., no energy stored) and no heat transfer via radiation, one obtains:

$$w = q_c + q_L \tag{29.28}$$

The heat transfer q_c due to natural and forced convection normally is expressed in terms of the heat transfer coefficient h as:

$$q_c = hA_v\left(T_e - T_a\right) \tag{29.29}$$

where $A_v = \pi dL$ is the external surface area of the velocity sensor. The electric power w usually is expressed as:

$$w = E_v^2 / R_v \tag{29.30}$$

where E_v is the voltage across the sensor, and R_v is its electric resistance.

For the industrial velocity sensor shown in Figure 29.17, q_L is the heat conducted from the end of the heated velocity sensor of length L to the remainder of the sensor's length. Most of this heat is convected away by the flowing fluid, and a small fraction is conducted to the probe stem. In the case of research hot-wire or cylindrical hot-film sensors, q_L is conducted to the two prongs, of which a major fraction is convected away and a minor fraction enters the probe stem. In well-designed velocity sensors, q_L is at most 10% to 15% of w, a fraction that decreases as velocity increases.

For research velocity sensors, the surface temperature T_e is identical to the wire or film temperature T_v. However, the surface temperature T_e of industrial velocity sensors with stainless-steel sheaths is slightly less than the temperature T_v of the platinum winding because a temperature drop is required to pass the heat q_c through the intervening "skin" — the cement layer and the stainless-steel tube. This is expressed as:

$$T_e = T_v - q_c R_s \tag{29.31}$$

where R_s is the thermal skin resistance in units of K W^{-1}. R_s is a constant for a given sensor and is the sum of the thermal resistances of the cement layer and the stainless-steel tube. For research velocity sensors, $R_s = 0$ and $T_e = T_v$ in Equation 29.31. In well-designed, sheathed, industrial velocity sensors, R_s is minimized and is approximately 1 K W^{-1}. As evidenced by Equation 29.31, the effect of skin resistance increases as velocity (i.e., q_c) increases. The effect is almost negligible at low velocity; but at high velocity, it is responsible for the characteristic droop in power vs. velocity flow-calibration curves.

Because the flow around cylinders in cross flow is confounded by boundary-layer separation and vortex shedding, it has defied analytical solution. Therefore, the film coefficient h in Equation 29.29 is found using empirical correlations. Correlations for h are expressed in terms of the following nondimensional parameters:

$$\mathrm{Nu} = \Im\left(\mathrm{Re},\ \mathrm{Pr},\ \mathrm{Gr},\ \mathrm{M},\ \mathrm{Kn}\right) \tag{29.32}$$

where Nu = hd/k = Nusselt number (the heat-transfer parameter)
Re = $\rho Vd/\mu$ = Reynolds number (the ratio of dynamic to viscous forces)
Pr = $\mu C_p/k$ = Prandtl number (the fluid properties parameter)
M = Mach number (the gas compressibility parameter)
Kn = Knudsen number (the ratio of the gas mean free path to d)

In the above, k is the fluid's thermal conductivity; μ is its viscosity; and C_p is its coefficient of specific heat at constant pressure. If one takes the practical case where: (1) natural convection is embodied in Re and Pr, (2) the velocity is less than one third the fluid's speed of sound (i.e., <100 m s^{-1} in ambient air), and (3) the flow is not in a high vacuum, then one can ignore the effects of Gr, M, and Kn, respectively. Thus,

$$\mathrm{Nu} = \Im\left(\mathrm{Re},\ \mathrm{Pr}\right) \tag{29.33}$$

Over the years, many attempts have been made to find universal correlations for the heat transfer from cylinders in cross flow. For an isothermal fluid at constant pressure, King [7] expresses Equation 29.33 as:

$$\mathrm{Nu} = A + B\mathrm{Re}^{0.5} \tag{29.34}$$

where A and B are empirical calibration constants that are different for each fluid and each temperature and pressure. Kramers [8] suggests the following correlation:

$$\mathrm{Nu} = 0.42\mathrm{Pr}^{0.2} + 0.57\mathrm{Pr}^{0.33}\mathrm{Re}^{0.50} \tag{29.35}$$

This correlation accounts for the variation in fluid properties (k, μ, and Pr) with temperature. Kramers [8] evaluates these properties at the so-called "film" temperature $(T_v + T_a)/2$, rather than at T_a itself. Another comprehensive correlation is given by Churchill and Bernstein [9]. Several other correlations are similar to Equation 29.35, but have exponents for the Reynolds number ranging from 0.4 to 0.6. Others have 0.36 and 0.38 for the exponent of the Prandtl number. Equations 29.34 and 29.35 are strictly valid only for hot-wire sensors with very high L/d ratios, in which case q_L and R_s are zero. The following universal correlation is suggested for real-world velocity sensors with variable fluid temperature and nonzero q_L and R_s:

$$\mathrm{Nu} = A + B\mathrm{Pr}^{0.33}\mathrm{Re}^{n} \tag{29.36}$$

where constants A, B, and n are determined via flow calibration. Equation 29.36 is applicable to most commercial industrial and research velocity sensors.

Combining Equations 29.28, 29.29, 29.30, and 29.36, and recognizing that $h = k\text{Nu}/d$, one obtains:

$$E_v^2 / R_v = \left(Ak + Bk\text{Pr}^{0.33}\text{Re}^n\right)\left(T_v - T_a\right) \tag{29.37}$$

where A and B are new constants. A, B, and n are determined via flow calibration and account for all nonidealities, including end conduction and skin resistance. Equation 29.37 is applicable to most commercial industrial and research velocity sensors. Manufacturers of industrial thermal anemometers can add other calibration constants to Equation 29.37 to enhance its correlation with flow-calibration data. The presence of end conduction means that the temperature of the velocity sensor varies with the axial coordinate y in Figure 29.19. The temperature T actually sensed by the velocity sensor is the *average* temperature over length L, or:

$$T_v = \left(1/L\right)\int_o^L T_v\left(y\right)\text{d}y \tag{29.38}$$

Bruun [1] presents an analytical solution for T_v (y) for hot-wire sensors. Equation 29.38 is the correct expression for T_v in Equation 29.37 and is so defined hereafter.

For fluid temperatures less than 200°C, the electric resistance of the RTD velocity and temperature sensors is usually expressed as:

$$R_v = R_{v0}\left[1 + \alpha_v\left(T_v - T_0\right)\right] \tag{29.39}$$

$$R_T = R_{T0}\left[1 + \alpha_T\left(T_T - T_0\right)\right] \tag{29.40}$$

where R_{v0} and R_{T0} are, respectively, the electric resistances of the velocity sensor and the temperature sensor at temperature T_0 (usually 0°C or 20°C), and α_v and α_T are the temperature coefficients of resistivity at temperature T_0. Additional terms are added to Equations 29.39 and 29.40 when fluid temperatures exceed 200°C. When evaluated at the fluid temperature T_a, the resistance R_a of the velocity sensor is:

$$R_a = R_{v0}\left[1 + \alpha_v\left(T_a - T_0\right)\right] \tag{29.41}$$

For applications with wide excursions in fluid temperature, additional terms are added to Equations 29.39–29.41. At 20°C, α_v and α_T are approximately 0.0036°C^{-1} for tungsten wire; 0.0038°C^{-1} for pure platinum wire; 0.0016°C^{-1} for 90% platinum + 10% rhodium wire; 0.0024°C^{-1} for platinum film; and 0.0040°C^{-1} for tungsten film. R_v and R_a are called the "hot" and "cold" resistances of the velocity sensor, respectively. The ratio R_v/R_a is called the "overheat ratio." For gas flows, sheathed industrial velocity sensors are operated at overheat ratios from 1.1 to 1.4 ($T_v - T_a$ = 30°C to 100°C). For gas flows, the overheat ratio of tungsten hot-wire and hot-film sensors are usually set to approximately 1.8 ($T_v - T_a$ = 200°C to 300°C) and 1.4 ($T_v - T_a$ = 150°C to 200°C), respectively. For water flows, the overheat ratio of hot-film sensors is approximately 1.05 to 1.10 ($T_v - T_a$ = 10°C to 20°C). Mikulla [6] shows the importance of the effect of overheat ratio on frequency response.

Combining Equations 29.39 and 29.41, one obtains:

$$T_v - T_a = \frac{R_v - R_a}{\alpha_v R_{v0}} \tag{29.42}$$

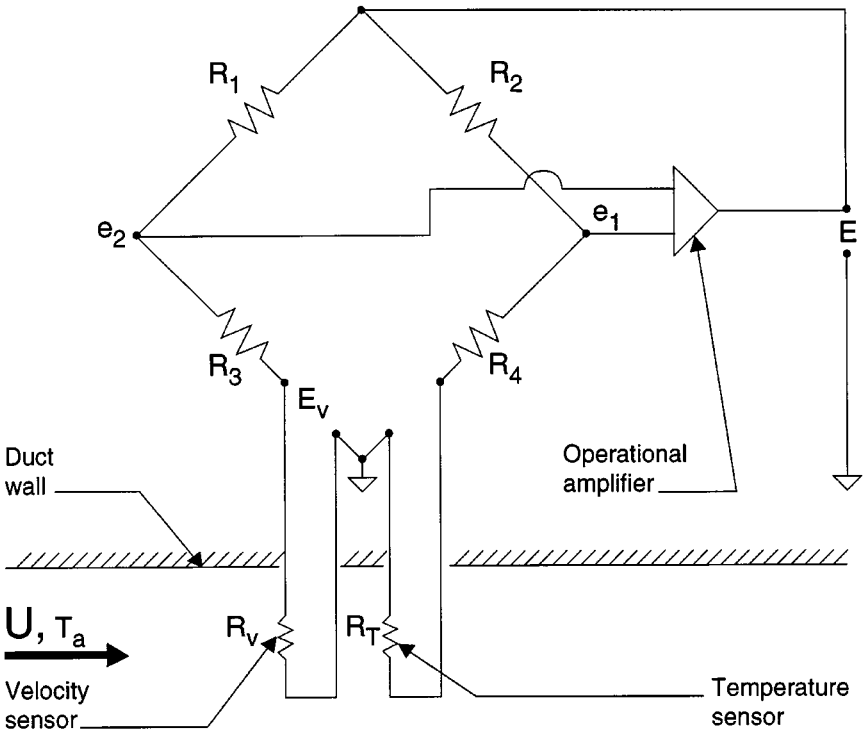

FIGURE 29.20 Constant-temperature thermal anemometer bridge circuit with automatic temperature compensation. R_1, R_2, and R_4 are fixed resistors selected to achieve temperature compensation; R_3 is the probe and cable resistance; R_v is the velocity sensor's resistance; R_T is the temperature sensor's resistance; and E is the bridge voltage output signal. For research anemometers operating in isothermal flows, the temperature sensor is eliminated and replaced with a variable bridge resistor. Some temperature compensation circuits have an additional resistor in parallel with R_T.

Inserting this into Equation 29.37 obtains:

$$\frac{E_v^2}{R_v\left(R_v - R_a\right)} = Ak + Bk\mathrm{Pr}^{0.33}\mathrm{Re}^n \tag{29.43}$$

where new constants A and B have absorbed the constants α_v and R_{v0}.

Figures 29.20 to 29.22 show three typical electronic drives for thermal anemometer sensors. Figure 29.20 shows the commonly used constant-temperature anemometer Wheatstone bridge circuit described by Takagi [10]. Figure 29.21 is similar, but is controlled and operated via a personal computer. In the constant-temperature mode, the hot resistance R_v, and hence the velocity sensor's temperature, remains virtually constant, independent of changes in velocity. With the addition of the temperature sensor shown in Figure 29.20, the bridge circuit also compensates for variations in fluid temperature T_a, as described later. Another common analog sensor drive is the constant-current anemometer. In this mode, a constant current is passed through the velocity sensor, and the sensor's temperature decreases as the velocity increases. Because the entire mass of the sensor must participate in this temperature change, the sensor is slower in responding to changes in velocity. Because the constant-temperature anemometer has a flatter frequency response, excellent signal-to-noise ratio [2], and is easier to use, it is favored over constant-current anemometers by most researchers and manufacturers for velocity and turbulence measurements. The constant-current anemometer with a very low overheat ratio is often used

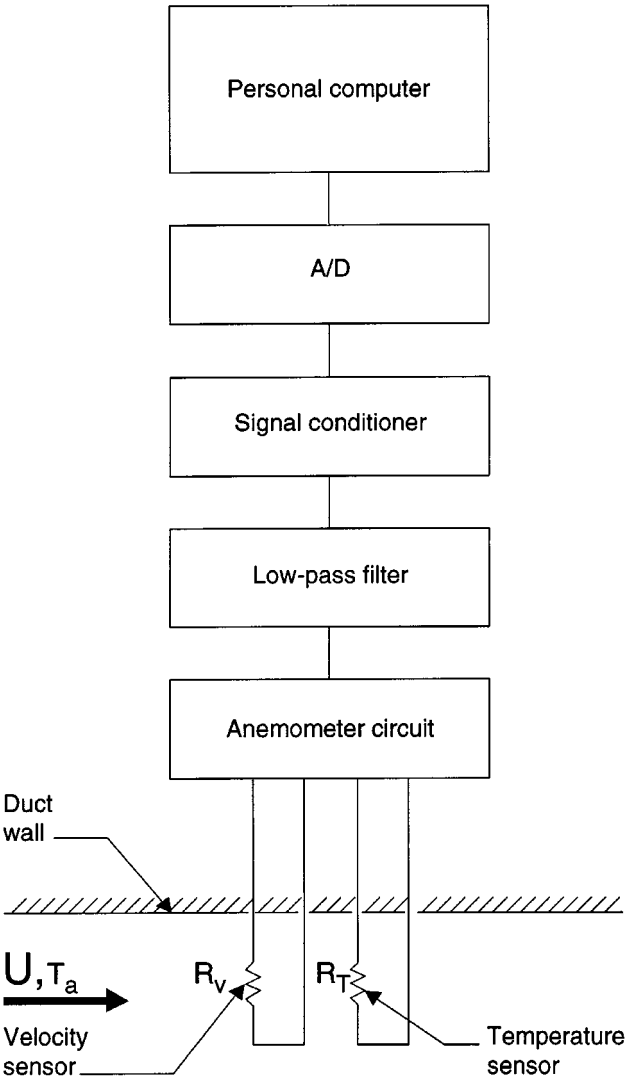

FIGURE 29.21 Personal computer-based digital thermal anemometer system. The signal conditioner matches the anemometer circuit's output to the ADC. For isothermal flows, the temperature sensor is eliminated.

as the temperature sensor. Subsequently, references made herein to sensor electronics will be based on the constant-temperature anemometer.

In the constant-temperature anemometer drive shown in Figure 29.20, the resistances R_1 and R_2 are chosen to: (1) maximize the current on the velocity-sensor side of the bridge so it becomes self-heated and (2) minimize the current on the temperature-sensor side of the bridge so it is not self-heated and is independent of velocity. Additionally, the temperature sensor must be sufficiently large in size to avoid self-heating. The ratio R_2/R_1 is called the "bridge ratio." A bridge ratio of 5:1 to 20:1 is normally used; but for optimum frequency response and compensation for long cable length, a bridge ratio of 1:1 can be used. In Figure 29.20, the operational amplifier, in a feedback control loop, senses the error voltage $(e_2 - e_1)$ and feeds the exact amount of current to the top of the bridge necessary to make $(e_2 - e_1)$ approach zero. In this condition, the bridge is balanced; that is,

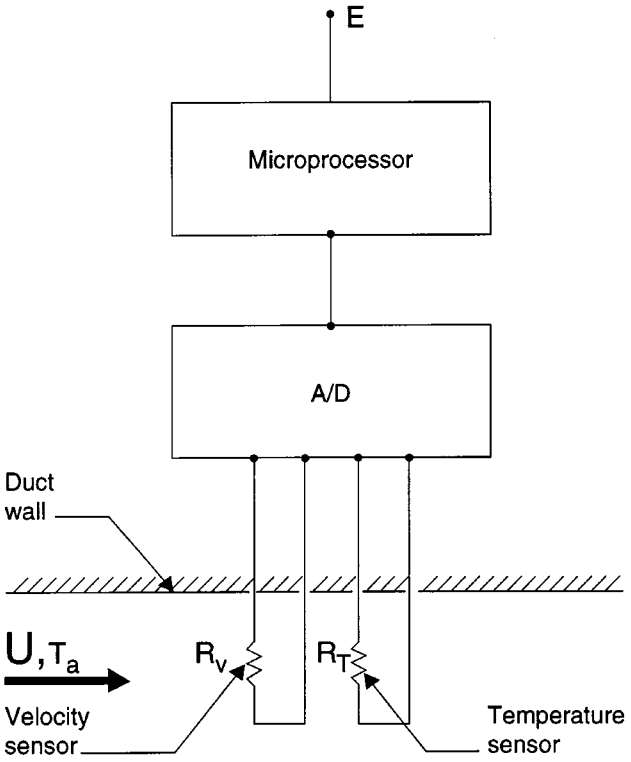

FIGURE 29.22 Microprocessor-based digital thermal anemometer. This system digitally maintains a constant temperature difference ($T_v - T_T$) and automatically corrects for the variation in fluid properties with temperature. The manufacturer provides a probe-mounted electronics package delivering an analog output signal E and/or a digital RS485 signal linearly proportional to gas mass velocity. (Reprinted with permission of Sierra Instruments, Inc.)

$$\frac{R_1}{R_v + R_3} = \frac{R_2}{R_T + R_4} \tag{29.44}$$

or

$$R_v = \frac{R_1}{R_2}\left(R_T + R_4\right) - R_3 \tag{29.45}$$

From Equation 29.45, one sees that R_v is a linear function of R_T. This relationship forms the basis for analog temperature compensation.

Expressing the voltage E_v across the velocity sensor in terms of the bridge voltage E, one obtains:

$$E_v = \frac{ER_v}{R_1 + R_3 + R_v} \tag{29.46}$$

Inserting this into Equation 29.43, one arrives at the generalized expression for the first law of thermodynamics for the thermal anemometer velocity sensor:

$$E^2 = G\left[Ak + Bk\left(\frac{\rho_s}{\mu}\right)^n \mathrm{Pr}^{0.33} U_s^n \right] \tag{29.47}$$

where $G = (R_1 + R_3 + R_v)^2 (R_v - R_a)/R_v$, and where A and B again are new constants. In Equation 29.47, one recognizes that conservation-of-mass considerations require that $\rho U = \rho_s U_s$, where ρ and U are referenced to the actual fluid temperature and pressure, and ρ_s and U_s are referenced to normal conditions of 0°C or 20°C temperature and 1 atm pressure. To write Equation 29.47 in terms of U, one simply replaces ρ_s by ρ and U_s by U.

Temperature Compensation

The objective of temperature compensation is to make the bridge voltage E in Equation 29.47 independent of changes in the fluid temperature T_a. This is accomplished if: (1) the term G in Equation 29.47 is independent of T_a and (2) compensation is made for the change in fluid properties (k, μ, and Pr) with T_a. Since these fluid properties have a weaker temperature dependence than G in Equation 29.47, for small temperature changes (less than ±10°C) in gas flows, only G requires compensation.

The two-temperature method is a typical procedure for compensating for both G and fluid properties. In this method, fixed-bridge resistors R_1, R_2, and R_4 in Figure 29.20 are selected so that E is identical at two different temperatures, but at the *same* mass flow rate. This procedure is accomplished during flow calibration and has variations among manufacturers.

The two-temperature method adequately compensates for temperature variations less than approximately ±50°C. In higher temperature gas flow applications, such as the flow of preheated combustion air and stack gas, temperature variations typically are higher. The microprocessor-based digital sensor drive in Figure 29.22 provides temperature compensation for temperature variations ranging from ±50°C to ±150°C. This sensor drive has no analog bridge. Instead, it has a virtual digital bridge that maintains $(T_v - T_a)$ constant within 0.1°C and has algorithms that automatically compensate for temperature variations in k, μ, and Pr. For this digital sensor drive, the first law of thermodynamics is found from Equation 29.37 as:

$$w = \left[Ak + Bk\left(\frac{\rho_s}{\mu}\right)^n \mathrm{Pr}^{0.33} U_s^n \right] \Delta T \tag{29.48}$$

where $\Delta T = (T_v - T_a)$ is now a known constant.

Flow Calibration

Figure 29.23 shows a typical flow calibration curve for the digital electronics drive shown in Figure 29.22. The curve is nonlinear of a logarithmic nature. The nonlinearity is disadvantageous because it requires linearization circuitry, but is advantageous because it provides rangeabilities up to 1000:1 for a single sensor. Additionally, the high-level output of several volts provides excellent repeatability and requires no amplification other than that for spanning. Since the critical dimensions of thermal anemometer sensors are so small, current manufacturing technology is incapable of maintaining sufficiently small tolerences to ensure sensor reproducibility. Therefore, each thermal anemometer must be flow calibrated, for example as in Figure 29.23, over its entire velocity range, either at the exact fluid temperature of its usage or over the range of temperatures it will encounter if it is to be temperature compensated. A 10 to 20 point velocity calibration is required to accurately determine the calibration constants A, B, and n in Equation 29.47. A least-squares curve-fitting procedure usually is applied. Proper flow calibration requires two critical elements: (1) a stable, reproducible, flow-generating facility and (2) an accurate velocity transfer standard. Bruun [1] and Gibbings et al. [4] provide more insight into curve fitting.

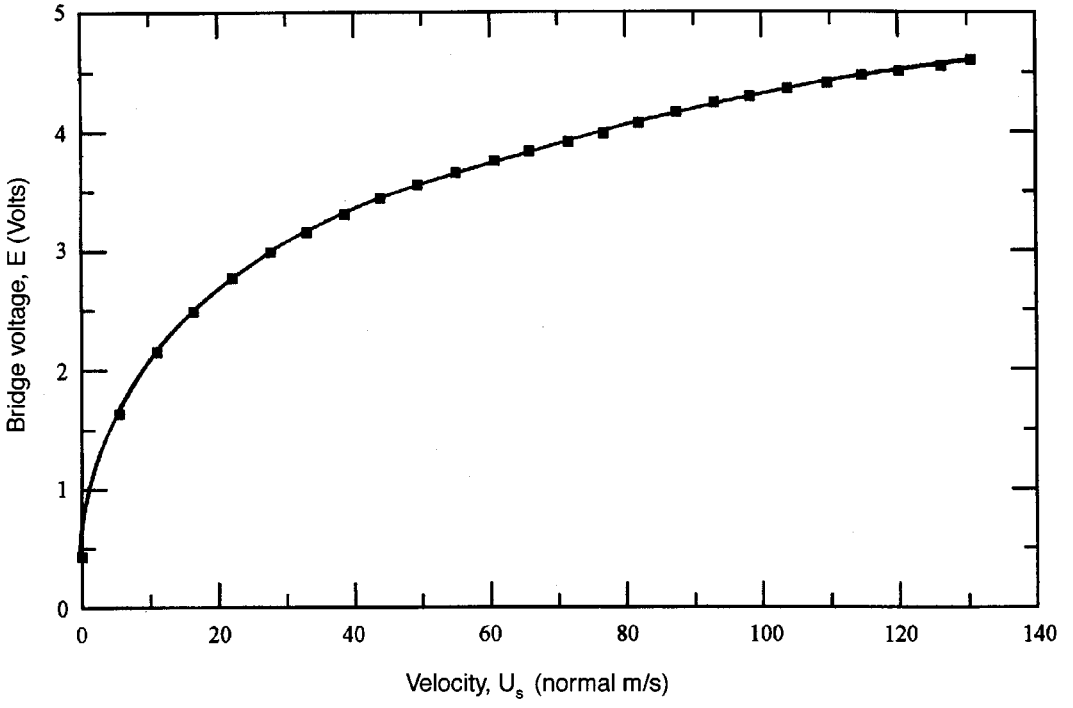

FIGURE 29.23 Typical flow calibration curve for an industrial thermal anemometer. The electronics drive is that shown in Figure 29.22. The constant temperature differential ($T_v - T_T$) is 50.0°C. The cold resistances R_{v0} and R_{T0} of the velocity and temperature sensors at 20°C are approximately 20 Ω and 200 Ω, respectively. (Reprinted with permission of Sierra Instruments, Inc.)

Flow-generating facilities are of two types — open loop and closed loop. An open-loop facility consists of: (1) a flow source such as a fan, pump, elevated tank, or compressed gas supply; (2) a flow-quieting section, such as a plenum with flow straighteners, screens, or other means to reduce swirling, turbulence, or other flow nonuniformities; (3) a nozzle to accelerate the flow and further flatten, or uniformize, the velocity profile; (4) a test section or free jet into which the thermal anemometer probe is inserted; and (5) a means for holding and sealing the thermal anemometer probe and velocity transfer standard. The test section or free jet must have: a velocity profile which is uniform within approximately 0.5% to 1.0% in its central portion; a turbulence intensity less than about 0.5%; and an area large enough so that the projected area of the velocity probe is less than 5% to 10% of the cross-sectional area. Manufacturers of small open-loop flow calibrators often determine the calibration flow velocity by measuring the pressure drop across the nozzle.

The closed-loop flow-generating facility, or wind tunnel, has the same components, but the exit of the test section is connected via ductwork to the inlet of the fan or pump so that the air mass inside the facility is conserved. Open-loop facilities are less expensive than closed-loop tunnels and are far more compact, making them suitable for flow calibrations in the field. But, a laboratory open-loop air-flow calibrator with a fan as the flow generator actually is *closed loop*, with the loop closing within the laboratory. For air velocities less than about 5 m s^{-1}, open-loop calibrators can experience shifts due to changing pressure, temperature, or other conditions in the laboratory. Properly designed closed-loop wind tunnels generate precise, reproducible air velocities from about 0.5 m s^{-1} to 150 m s^{-1}. When fitted with water chillers, they remove compression heating and provide a constant-temperature air flow within ±2°C. When fitted with an electric heater and proper thermal insulation, they provide air temperatures up to 300°C. Gibbings [4] describes a water box displacement rig for flow calibration at very low velocities in the range of 0.1 m s^{-1} to 4 m s^{-1}.

Pitot tubes and laser Doppler anemometers are the two most common velocity transfer standards used to calibrate thermal anemometers. Both have detailed descriptions earlier in this chapter. The Pitot tube usually has the classical "L" shape and an outside diameter of about 3 mm. Its tip is located in the same plane in the test section as the thermal anemometer probe but is no closer than approximately 3 cm. The focal volume of the laser Doppler anemometer is similarly located. The Pitot tube is far less expensive and easier to operate, but is difficult to use if air velocities are less than about 3 m s^{-1}. A proper Pitot-tube flow transfer standard should have its calibration recertified every 6 months by an accredited standards laboratory. On the other hand, the laser Doppler anemometer is a fundamental standard that accurately measures air velocity from approximately 0.5 m s^{-1} to 100 m s^{-1}. Since it provides noncontact anemometry, it is usable at high temperatures. Its primary disadvantages are high expense and complications associated with properly seeding the flow with particles.

Measurements

Point Velocity

Based on the first law of thermodynamics expressed by Equation 29.47, one now can solve for the desired quantity — either the actual point velocity U (m s^{-1}) or the point mass velocity U_s (normal m s^{-1}). Here, one assumes that the velocity vector is normal to the flow sensor. Two- and three-dimensional velocity measurements are discussed later. In the following, A, B, and n are constants, but are different for each case.

The simplest case is isothermal flow with a hot-wire sensor having a very high length-to-diameter ratio (L/d). In this case, the exponent n in Equation 29.47 is 0.5, as shown by Equation 29.34. The applicable first law and velocity expressions are:

$$E^2 = A + BU^{0.5} \tag{29.49}$$

and

$$U = \left[\frac{E^2 - A}{B}\right]^2 \tag{29.50}$$

In the case of a real-world sensor in an isothermal flow having either end loss only or both end loss and skin resistance, one obtains:

$$E^2 = A + BU^{n} \tag{29.51}$$

and

$$U = \left[\frac{E^2 - A}{B}\right]^{1/n} \tag{29.52}$$

Often, Equation 29.52 is replaced with a polynomial of the form $U = F(E^2)$, where the function $F(\ )$ is a fourth-order polynomial whose coefficients are determined from flow calibration data using least-squares curve-fitting software. For the same case as above, but with nonisothermal flow, the first law is expressed by Equation 29.47, and the velocity is expressed as:

$$U_s = \frac{\mu}{\rho_s}\left[\frac{E^2/G - Ak}{Bk\mathrm{Pr}^{0.33}}\right]^{1/n} \tag{29.53}$$

For the digital sensor drive of Figure 29.22, the first law is given by Equation 29.48, and the velocity by:

$$U_s = \frac{\mu}{\rho_s}\left[\frac{w/\Delta T - Ak}{Bk\mathrm{Pr}^{0.33}}\right]^{1/n} \tag{29.54}$$

Current commercial industrial thermal anemometer systems have temperature-compensation and "linearization" electronics that automatically calculate U_s as a linear function of E or w, based on the foregoing relationships.

Turbulence

Turbulence measurements are the second most common application of research thermal anemometers. This measurement requires the high-freqency response of hot-wire and hot-film research anemometers operated in the constant-temperature mode. The vast majority of fluid flows are turbulent. Only flows with very low Reynolds numbers are nonturbulent, or laminar. Turbulent flows are time variant and usually are separated as follows into time-mean and fluctuating parts:

$$\begin{aligned} U(t) &= U + u \\ V(t) &= \overline{V} + v \\ W(t) &= \overline{W} + w \\ T_a(t) &= \overline{T}_a + \theta \\ E &= E + e \end{aligned} \tag{29.55}$$

where $U(t)$, $V(t)$, $W(t)$ are the orthogomal components in the x, y, and z directions, respectively, such as shown in Figure 29.18 for the 3-D hot-wire probe. T_a (t) is the fluid temperature, and $E(t)$ is the bridge voltage. $\overline{U}$, $\overline{W}$, $\overline{V}$, $\overline{T}_a$, and $\overline{E}$ are the time-mean parts, and $u(t)$, $v(t)$, $w(t)$, $\theta(t)$, and $e(t)$ are the time-dependent fluctuating parts. The time-mean parts are averaged sufficiently long to become independent of turbulent fluctuations, yet respond to changes with time in the main flow. In the previous subsection, the expressions given were for the time-mean velocity. In the study of turbulence, one is primarily interested in the time average of the product of two fluctuating velocity components (turbulence correlations) because these terms appear in the time-averaged Navier–Stokes equation. Two important turbulence correlations are $\overline{u^2}$ and $\overline{uv}$. The correlation $(\sqrt{\overline{u^2}})/\overline{U}$ is called the *turbulence intensity*. Manufacturers of research anemometer systems provide electronics for automatically computing turbulence correlations.

For a fluid with changes in temperature sufficiently small that fluid properties are essentially constant, one can write Equation 29.47 in the following form:

$$E^2 = \left(A + BU^n\right)\left(T_v - T_a\right) \tag{29.56}$$

where A, B, and n are constant and where R_v is virtually constant because the anemometer is in the constant-temperature mode. Elsner [11] shows that the fluctuating voltage e is found by taking the total derivative of Equation 29.56, as follows:

$$e = S_u u + S_\theta \theta \tag{29.57}$$

where

$$S_u = \frac{\delta E}{\delta U} = \frac{nBU^{n-1}}{2}\left[\frac{\left(T_v - T_a\right)}{A + BU^n}\right]^{1/2} = \textit{Velocity sensitivity} \tag{29.58}$$

$$S_\theta = \frac{\delta E}{\delta T_a} = -\frac{1}{2}\left[\frac{\left(A + BU^n\right)}{\left(T_v - T_a\right)}\right]^{1/2} = \textit{Temperature sensitivity} \tag{29.59}$$

It is seen from Equations 29.58 and 29.59 that increasing $(T_v - T_a)$, i.e., operating the sensor as hot as possible, maximizes the velocity sensitivity and minimizes the sensitivity to temperature fluctuations. This is why tungsten hot wires are operated at high temperatures (typically 200°C to 300°C).

The fluctuating components of velocity have a broad frequency spectrum, ranging from 10^{-2} Hz to 10^5 Hz, and sometimes even higher. Therefore, it is imperative that the frequency response of constant-temperature research anemometers have a flat frequency response, i.e., minimized attenuation and phase shift at higher frequencies. Blackwelder [12] and several other investigators have studied the frequency response of hot-wire anemometers. For turbulence measurements, Borgos [13] describes commercial research anemometer systems with features such as: low-pass filters to decrease electronics noise; a subcircuit for determining and setting overheat ratio; a square-wave generator for frequency response testing; and two or more controls to optimize the frequency response to fast fluctuations. Recent systems have electronics that compensate for frequency attenuation. When used with 5 μm diameter hot-wire sensors in air, commercial systems are capable of nearly flat frequency response and very small phase lag from 0 Hz to approximately 10^4 Hz. As reported by Nelson and Borgos [14], wedge and conical hot-film sensors in water have a relatively flat response from 0 Hz to 10 Hz for velocities above 0.3 m s^{-1}.

Two- and three-component velocity and turbulence measurements are made using hot-wire or hot-film research anemometers, such as shown in Figure 29.18. As described by Müller [15], hot-wire or cylindrical hot-film probes in the "X"-configuration are used to measure the *U* and *V* velocity components. In a three-sensor orthogonal array, they measure *U*, *V*, and *W*. Döbbeling, Lenze, and Leuckel [16] and other investigators have developed four-wire arrays for measurement of *U*, *V*, and *W*. Olin and Kiland [17] describe an orthogonal array of three cylindrical split hot-film sensors. Each of the three sensors in this array has two individually operated hot-films separated by two axial splits 180° apart along its entire length. The two split films take advantage of the nonuniform heat-transfer distribution around a cylinder in cross flow.

In multisensor arrays, the velocity vector is not necessarily normal to a cylindrical sensor. If the discussion is limited to isothermal flows, the first law expressed by Equation 29.47 becomes:

$$E^2 = A + BV_e^n \tag{29.60}$$

where V_e is the effective velocity sensed by a single cylindrical sensor in the array, and *A*, *B*, and *n* are constants. Jörgenson [18] describes V_e as follows:

$$V_e^2 = U_N^2 + a^2\, U_T^2 + b^2\, U_B^2 \tag{29.61}$$

where U_N = velocity component normal to the sensor
U_T = tangential component
U_B = component perpendicular to both U_N and U_T (i.e., binormal)

The constants a and b in Equation 29.61 are referred to as the sensor's yaw and pitch coefficients, respectively, and are determined via flow calibration. Typical values for a and b for a plated hot-wire sensor are 0.2 and 1.05, respectively. Inserting Equation 29.61 into Equation 29.60, we get the following expression for the output signal of a single sensor in the array:

$$E^2 = A + B\left(U_N^2 + a^2 U_T + b^2 U_B^2\right)^{n/2} \tag{29.62}$$

Expressions like this, or similar ones such as given by Lekakis, Adrian, and Jones [19], are written for all sensors in the array. These expressions and trigonometry are then used to solve for the components of velocity U, V, and W in the x, y, z spatially fixed reference frame.

Channel Flows

Based on the following relationship, a single-point industrial *insertion* thermal anemometer monitors the mass flow rate $\dot{m}$ (kg s^{-1}) in ducts, pipes, stacks, or other flow channels by measuring the velocity $U_{s,c}$ at the channel's centerline:

$$\dot{m} = \rho_s \gamma\, U_{s,c} A_c \tag{29.63}$$

where $U_{s,c}$ is the velocity component parallel to the channel's axis measured at the channel's centerline and referenced to *normal* conditions of 0°C or 20°C temperature and 1 atmosphere pressure; ρ_s, a constant, is the fluid's mass density at the same normal conditions; A_c, another constant, is the cross-sectional area of the channel; and γ is a constant defined as $\gamma = U_{s,ave}/U_{s,c}$, where $U_{s,ave}$ is the average velocity over area A_c. The velocity in channel flows is seldom uniform and therefore γ is not unity. If the flow channel has a length-to-diameter ratio of 40 to 60, then its flow profile becomes unchanging and is called "fully developed." In fully developed flows, the fluid's viscosity has retarded the velocity near the walls, and hence γ is always less than unity. If the channel's Reynolds number is less than 2000, the flow is laminar; the fully developed profile is a perfect parabola; and γ is 0.5. If the Reynolds number is larger than 4000, the flow is turbulent; the fully developed profile has a flattened parabolic shape; and for pipes with typical rough walls, γ is 0.79, 0.83, and 0.83 for Reynolds numbers of 10^4, 10^5, and 10^6, respectively. If the Reynolds number is between 2000 and 4000, the flow is transitioning between laminar and turbulent flows, and γ ranges between 0.5 and 0.8.

Unfortunately, in most large ducts and stacks, 40 to 60 diameters of straight run preceding the flow monitoring location does not exist. Instead, the flow profile usually is highly nonuniform, swirling, and, in air-preheater ducts and in stacks, is further confounded by temperature nonuniformities. In these cases, single-point monitoring is ill-advised. Fortunately, multipoint monitoring with industrial thermal anemometer flow-averaging arrays, such as shown in Figure 29.18, have proven successful in these applications. As described by Olin [20], this method consists of a total of N (usually, $N = 4$, 8, or 12) industrial thermal anemometer sensors, each similar to that shown in Figure 29.17, located at the centroid of an equal area A_c/N in the channel's cross-sectional area A_c. The individual mass flow rate $\dot{m}_i$ monitored by each sensor is $\rho_s\, U_{s,i}\, (A_c/N)$, where $U_{s,i}$ is the individual velocity monitored by the sensor at point i. The desired quantity, the total mass flow rate $\dot{m}$ through the channel, is the sum of the individual mass flow rates, or:

$$\dot{m} = \sum_{i=1}^{N} \dot{m}_i = \rho_s A_c U_{s,ave} \tag{29.64}$$

where $U_{s,ave}$ is the arithmetic average of the N individual velocities $U_{s,i}$. As described by Olin [21], industrial multipoint thermal anemometers are used as the flow monitor in stack continuous emissions monitoring systems required by governmental air-pollution regulatory agencies.

Table 29.3 Typical Commercial Thermal Anemometer Systems

Product Description	Average 1997 U.S. List Price
Industrial systems	
Insertion mass flow transducer	$1,900
50 mm (2 in.) NPT in-line mass flowmeter	$2,500
8-point smart industrial flow averaging array	$15,000
Research systems	
Single-channel hot-wire or hot-film anemometer system	$10,000
Three-component hot-wire anemometer system	$21,000
Portable air velocity meter	$1,000

Note: Prices listed are the average of the manufacturers listed in Table 29.4. Insertion probe is 25 cm in length. Insertion and in-line mass flowmeters have: probe-mounted FM/CENELEC approved, explosion-proof housing; ac line voltage input power; 5-0 V dc output signal; 316 SS construction; and ambient air calibration. In-line industrial mass flowmeter has built-in flow conditioning. Industrial flow averaging array has four 1 m long probes, 2 points per probe, 316 SS construction, line voltage input power, 0 to 5 V dc output signal, and smart electronics mounted on probe. Research anemometer systems have standard hot-wire probes, most versatile electronics, and include ambient air calibrations.

TABLE 29.4 Manufacturers of Thermal Anemometer Systems

Industrial Systems and Portable Air Velocity Meters

Sierra Instruments, Inc.
5 Harris Court
Building L
Monterey, CA 93940
Tel: (831) 373-0200
Fax: (831) 373-4402

Fluid Components, Inc.
1755 La Costa Meadows Drive
San Marcos, CA 92069
Tel: (619) 744-6950
Fax: (619) 736-6250

Kurz Instruments, Inc.
2411 Garden Road
Monterey, CA 93940
Tel: (831) 646-5911
Fax: (831) 646-8901

Research Systems and Portables

TSI Inc.
500 Cardigan Road
St. Paul, MN 55164
Tel: (612) 490-2811
Fax: (612) 490-3824

Dantec Measurement Technology, Inc.
Denmark
Tel: (45) 4492 3610
Fax: (45) 4284 6136

Instrumentation Systems

Table 29.3 lists examples of typical commercial thermal anemometer systems. Table 29.4 lists their major manufacturers. Thermal anemometer systems include three elements: sensors, probe, and electronics. Sensors and probes have been described in previous sections. The electronics of industrial systems are enclosed in an explosion-proof or other industrial-grade housing mounted either directly on the probe or remotely (usually within 30 m). The electronics is powered with a 24 V dc source or with 100, 115, or 230 V ac line voltage. The output signal typically is 0 to 5 V dc, 4 to 20 mA, RS232, or RS485 linearly proportional to gas mass velocity U_s over the range of 0.5 normal m s^{-1} to 150 normal m s^{-1}. In-line mass

flowmeters have the same output-signal options and are calibrated directly in mass flow rate $\dot{m}$ (kg s^{-1}). In-line meters are now available with built-in flow conditioners that eliminate errors associated with upstream disturbances, such as elbows, valves, and pipe expansions. Systems are available either with lower cost analog electronics or with smart microprocessor-based electronics. The repeatability of these systems is ±0.2% of full scale. The typical accuracy of a smart industrial system is ±2% of reading over 10 to 100% of full scale and ±0.5% of full scale below 10% of full scale. Automatic temperature compensation facilitates temperature coefficients of ±0.04% of reading per °C within ±20°C of calibration temperature and ±0.08% of reading per °C within ±40°C. High-temperature applications have temperature compensation over a range of ±150°C. Pressure effects are negligible within ±300 kPa of calibration pressure.

Research thermal anemometer systems usually are coupled with a personal computer, as shown in Figure 29.21. The PC provides system set-up and control, as well as data display and analysis. Modern systems feature low-noise circuits, together with smart bridge optimization technology that eliminates tuning and automatically provides flat frequency response up to 300,000 Hz. Lower cost units provide flat response up to 10,000 Hz. A built-in thermocouple circuit simplifies temperature measurement. The PC's windows-based software provides near real-time displays of velocity, probability distribution, and turbulence intensity. Post-processing gives additional statistics, including: mean velocity; turbulence intensity; standard deviation; skewness; flatness; normal stress for one-, two-, and three-component probes; as well as shear stress, correlation coefficients and flow-direction angle for two- and three-dimensional probes. In addition, power spectrum, auto correlations, and cross correlations can be displayed. The software automatically handles flow calibration set-up and calculates calibration velocity. Systems are available in 1-, 2-, 8-, and 16-channel versions.

Commercial industrial and research thermal anemometer systems were first introduced in the early 1960s. At first, industrial thermal anemometers were not considered sufficiently durable for the rigors of industrial use. With the advent of stainless-steel sheathed sensors and microprocessor-based electronics, industrial thermal anemometers now enjoy the credibility formerly attributed to only traditional flowmeter approaches. Initial research systems required a high level of user knowledge and considerable involvement in operation. In contrast, current research systems have nearly flat frequency response, high accuracy, and easy-to-use controls providing the flexibility researchers require. Research systems based on personal computers have graphical user interfaces that enhance both performance and simplicity of operation.

References

1. H. H. Bruun, *Hot-Wire Anemometry: Principles and Signal Analysis,* Oxford: Oxford University Press, 1995.
2. L. M. Fingerson and P. Freymuth, Thermal anemometers, in R. J. Goldstein (ed.), *Fluid Mechanics Measurements,* Washington, D.C.: Hemisphere, 1983.
3. P. Freymuth, History of thermal anemometry, in N.P. Cheremisinoff and R. Gupta (ed.), *Handbook of Fluids in Motion,* Ann Arbor, MI: Ann Arbor Science Publishers, 1983.
4. J. C. Gibbings, J. Madadnia, and A.H. Yousif, The wall correction of the hot-wire anemometer, *Flow Meas. Instrum.,* 6(2), 127-136, 1995.
5. J. C. Gibbings, J. Madadnia, S. Riley, and A.H. Yousif, The proximity hot-wire probe for measuring surface shear in air flows, *Flow Meas. Instrum.,* 6(3), 201-206, 1995.
6. V. Mikulla, *The Measurement of Intensities and Stresses of Turbulence in Incompressible and Compressible Air Flow,* Ph.D. Thesis, University of Liverpool, 1972.
7. L. V. King, On the convection of heat from small cylinders in a stream of fluid: determination of the convection constants of small platinum wires with application to hot-wire anemometry, *Phil. Trans. Roy. Soc.,* A214, 373-432, 1914.
8. H. Kramers, Heat transfer from spheres to flowing media. *Physica*, 12, 61-80, 1946.

9. S. W. Churchill and M. Bernstein, A correlating equation for forced convection from gases and liquids to a circular cylinder in crossflow, *J. Heat Transfer*, 99, 300-306, 1997.
10. S. Takagi, A hot-wire anemometer compensated for ambient temperature variations, *J. Phys. E.: Sci. Instrum.*, 19, 739-743, 1986.
11. J. W. Elsner, An analysis of hot-wire sensitivity in non-isothermal flow, *Proc. Dynamics Flow Conf., Marseille,* 1972.
12. R. F. Blackwelder, Hot-wire and hot-film anemometers, in R.J. Emrich (ed.), *Methods of Experimental Physics: Fluid Dynamics*, New York: Academic Press, 18A, 259-314, 1981.
13. J. A. Borgos, A review of electrical testing of hot-wire and hot-film anemometers, *TSI Quart.*, VI(3), 3-9, 1980.
14. E.W. Nelson and J. A. Borgos, Dynamic response of conical and wedge type hot films: comparison of experimental and theoretical results, *TSI Quart.*, IX(1), 3-10, 1983.
15. U. R. Müller, Comparison of turbulence measurements with single, X and triple hot-wire probes, *Exp. in Fluids*, 13, 208-216, 1992.
16. K. Döbbeling, B. Lenze, and W. Leuckel, Four-sensor hot-wire probe measurements of the isothermal flow in a model combustion chamber with different levels of swirl, *Exp. Thermal and Fluid Sci.*, 5, 381-389, 1992.
17. J.G. Olin and R. B. Kiland, Split-film anemometer sensors for three-dimensional velocity-vector measurement, *Proc. Symp. on Aircraft Wake Turbulence*, Seattle, Washington, 1970, 57-79.
18. F. E. Jörgenson, Directional sensitivity of wire and fibre-film probes, *DISA Info.*, (11), 31-37, 1971.
19. I. C. Lekakis, R. J. Adrian, and B. G. Jones, Measurement of velocity vectors with orthogonal and non-orthogonal triple-sensor probes, *Experiments in Fluids,* 7, 228-240, 1989.
20. J. G. Olin, A thermal mass flow monitor for continuous emissions monitoring systems (CEMS), *Proc. ISA/93 Int. Conf. Exhibition & Training Program*, (93-404), 1993, 1637-1653.
21. J. G. Olin, Thermal flow monitors take on utility stack emissons, *Instrumentation and Control Systems*, 67(2), 71-73, 1994.

Further Information

J. A. Fay, *Introduction to Fluid Mechanics,* Cambridge, MA: MIT Press, 1994.
A. Bejan, *Convection Heat Transfer,* New York: John Wiley & Sons, 1995.

29.3 Laser Anemometry

Rajan. K. Menon

Laser anemometry, or *laser velocimetry*, refers to any technique that uses lasers to measure velocity. The most common approach uses the Doppler shift principle to measure the velocity of a flowing fluid at a point and is referred to as Laser Doppler Velocimetry (LDV) or Laser Doppler Anemometry (LDA). This technique (also known as dual beam, differential Doppler or fringe mode technique), incorporating intersecting (focused) laser beams, is also used to measure the motion of surfaces [1]. In some special flow situations, another approach using two *nonintersecting*, focused laser beams known as *dual focus* (also known as L2F) technique is used to measure flow velocity at a point [2]. More recently, laser illumination by light sheets is used to make global flow measurements and is referred to as *particle image velocimetry* (PIV) [3]. The strength of PIV (including particle tracking velocimetry) lies in its ability to capture turbulence structures within the flow and transient phenomena, and examine unsteady flows [4]. The development of this technique to obtain both spatial and temporal information about flow fields is making this a powerful diagnostic tool in fluid mechanics research [5, 6]. Other approaches to measure

global flow velocities come under the category of molecular tagging velocimetry [7] or Doppler global velocimetry [8, 9].

The noninvasive nature of the LDV technique and its ability to make accurate velocity measurements with high spatial and temporal resolution, even in highly turbulent flows, have led to the widespread use of LDV for flow measurement. Flow velocities ranging from micrometers per second to hypersonic speeds have been measured using LDV systems. Measurements of highly turbulent flows [10], flows in rotating machinery [11], especially in the interblade region of rotors [12, 13], very high [14] or very low [15] velocity flows, flows at high temperatures [16] and in other hostile environments [17, 18], and flows in small spaces [19] have been performed using the LDV technique. The versatility and the widespread use of the LDV approach to measure flows accurately has resulted in referring to this technique as *laser velocimetry* or *laser anemometry*. Many details of the technique, including some of the early developments of the hardware, are provided in the book by Durst [20]. A bibliography of the landmark papers in LDV has been compiled by Adrian [21].

For the case of spherical scatterers, the technique has also been extended to measure size of these particles. In this case, the scattered light signal from a suitably placed receiver system is processed to obtain the diameter of the particle, using the phase Doppler technique [22].

The first reported fluid flow measurements using LDV principles was by Yeh and Cummins [23]. Although in this case an optical arrangement referred to as the reference beam system was used to measure the Doppler shift, in almost all measurement applications, what is referred to as the dual beam or differential Doppler arrangement [24] is used now. This arrangement, also referred to as the "fringe" mode of operation, uses two intersecting laser beams (Figure 29.24) to measure one velocity component.

The advantages of the LDV technique in measuring flows include (1) a small measuring region (i.e., point measurement), (2) high measurement accuracy, (3) the ability to measure any desired velocity component, (4) accurate measurement of high turbulence intensities, including flow reversals, (5) a large dynamic range, (6) no required velocity calibration, (7) no probe in the flow (does not disturb the flow; measures in hostile environments), and (8) good frequency response.

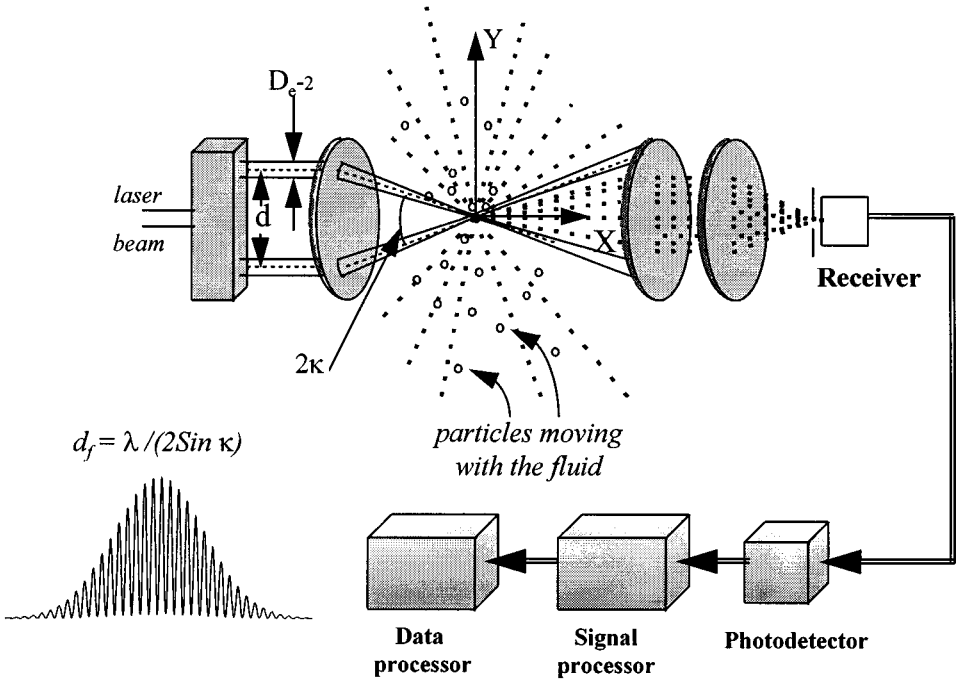

FIGURE 29.24 Schematic of a dual-beam system.

The LDV technique relies on the light scattered by scattering centers in the fluid to measure flow velocity. These scattering centers will also be referred to as *particles*, with the understanding that bubbles or anything else that has a refractive index different from that of the fluid could be the source of scattered light. The particles, whose velocities are measured, must be small enough (generally in the micron range) to follow the flow variations and large enough to provide signal strength adequate for the signal processor to give velocity measurements. It should be noted that the signal exists only when a "detectable" particle is in the measuring volume and, hence, is discontinuous. This, along with other properties of the signal, adds special requirements on the signal processing and the subsequent data analysis systems. The scattered light signal is processed to obtain the Doppler shift frequency and from that the velocity of the particle. Hence, the rate at which the velocity measurements are made depends on the rate of particle arrival. It is desirable to have a high particle concentration to obtain a nearly continuous update of velocity. In carefully controlled experiments, the LDV system can provide very high accuracy (0.1% or better) measurements in mean velocity. Thermal anemometer systems are generally able to measure lower turbulence levels compared to that by an LDV system [25]. While the direct measurement of the Doppler-shifted frequency from a single laser beam caused by a moving particle is possible [26], most LDV systems employ the heterodyne principle to obtain and process only the Doppler shift (difference) frequency.

Principle of Operation

Dual-Beam Approach

The dual-beam approach is the most common optical arrangement used for LDV systems for flow measurement applications. The schematic (Figure 29.24) shows the basic components of a complete LDV system to measure one component of velocity. The transmitting optics include an optical element to split the original laser beam into two parallel beams and a lens system to focus and cross the two beams. The intersection region of the two beams becomes the measuring region. The receiving optics (shown to be set up in the forward direction) collect a portion of the light scattered by the particles, in the fluid stream, passing through the beam-crossing region (measuring volume) and direct this light to a photodetector, which converts the scattered light intensity to an analog electrical signal. The frequency of this signal is proportional to the velocity of the particle. A signal processor extracts the frequency information from the photodetector output and provides this as a digital number corresponding to the instantaneous velocity of the particle. The data processing system obtains the detailed flow properties from these instantaneous velocity measurements. The idealized photodetector signal, for a particle passing through the center of the measuring volume, is shown in the lower left side of Figure 29.24. Actual signals will have noise superimposed on them; and the signal shape will vary, depending on the particle trajectory through the measuring volume [27].

Fringe Model Description.

While there are several ways to describe the features of a dual-beam system, the description based on a fringe model is, perhaps, the simplest. For simplicity, the diameter and the intensity of both the beams are assumed to be the same. After the beams pass through the transmitting lens, the diameter of each beam continuously decreases to a minimum value (beam waist) at the focal point of the lens, and then increases again. Thus, the beam waists cross where the two laser beams intersect (at the focal point of the lens), and the wavefronts in the beams interfere with each other, creating a fringe pattern [28]. In this pattern, assuming equal intensity beams and other needed qualities of the beams, the light intensity varies from zero (dark fringe) to a maximum (bright fringe), and the fringes are equally spaced. The particles in the flow passing through the intersection region (measuring region) scatter light in all directions. An optical system, including a receiving lens (to collimate the scattered light collected) and a focusing lens, is used to collect the scattered light and focus it onto the receiver. The aperture in front of the receiver is used to block out stray light and reflections and collect only the light scattered from the measuring region.

As a particle in the flow, with velocity u, moves across the fringes, the intensity pattern of the light scattered by the particle resembles that shown in the lower left of Figure 29.24. The velocity component,

u_y (perpendicular to the optical axis and in the plane of the incident beams) can be obtained from the ratio of the distance between fringes (or fringe spacing, d_f), and the time t (= $1/f_D$) for the particle to cross one pair of fringes, where f_D is the frequency of the signal. The amplitude variation of the signal reflects the Gaussian intensity distribution across the laser beam. Collection (receiving) optics for the dual-beam system can be placed at any angle, and the resulting signal from the receiving system will still give the same frequency. However, signal quality and intensity will vary greatly with the collection optics angle.

Doppler Shift Explanation.
The description of the dual-beam system using the Doppler shift principle is as follows. At the receiver, the frequencies of the Doppler-shifted light scattered by a particle from beam one and beam two are given by:

$$\nu_{D1} = \nu_{01} + \frac{\vec{u}}{\lambda}\left(\hat{r} - \hat{S}_1\right); \quad \nu_{D2} = \nu_{02} + \frac{\vec{u}}{\lambda}\left(\hat{r} - \hat{S}_2\right) \tag{29.65}$$

where ν_{01} and ν_{02} are the frequencies of laser beam 1 and laser beam 2; $\hat{r}$ is the unit vector directed from the measuring volume to the receiving optics; $\hat{S}_1$ and $\hat{S}_2$ are the unit vectors in the direction of incident beam 1 and incident beam 2; $\vec{u}$ is the velocity vector of the particle (scattering center); and λ is the wavelength of light. The frequency of the net (heterodyne) signal output from the photodetector system is given by the difference between ν_{D1} and ν_{D2}.

$$f_D = f_S + \frac{\vec{u}}{\lambda}\left(\hat{S}_2 - \hat{S}_1\right) \tag{29.66}$$

where $f_S = \nu_{01} - \nu_{02}$ is the difference in frequency between the two incident beams. This difference frequency is often intentionally imposed (see section on frequency shifting) to permit unambiguous measurement of flow direction and high-turbulence intensities. Assuming $f_S = 0$, the frequency detected by the photodetector is:

$$f_D = \frac{\dot{u}}{\lambda}\left(\hat{S}_2 - \hat{S}_1\right) = 2u_y \sin\kappa \tag{29.67}$$

Hence,

$$u_y = \frac{f_D \lambda}{2\sin\kappa} = f_D\, d_f \tag{29.68}$$

This is the equation for u_y and shows that the signal frequency f_D is directly proportional to the velocity u_y. The heterodyning of the scattered light from the two laser beams at the photodetector actually gives both the sum and difference frequency. However, the sum frequency is too high to be detected and so only the difference frequency ($\nu_{D1} - \nu_{D2}$) is output from the photodetector as an electrical signal. The frequency f_D is often referred to as the Doppler frequency of the output signal, and the output signal is referred to as the Doppler signal.

It can be seen from Equation 29.68 that the Doppler frequency is independent of the receiver location ($\hat{r}$). Hence, the receiver system location can be chosen based on considerations such as signal strength, ease of alignment, and clear access to the measuring region. The expressions for the other optical configurations can be reduced similarly [29], giving the identical equation for the Doppler shift frequency f_D. It should be noted that the fringe description does not involve a "Doppler shift" and is, in fact, not always appropriate. The fringe model is convenient and gives the correct expression for the frequency. However, it can be misleading when studying the details of the Doppler signal (e.g., signal-to-noise ratio) and other important parameters e.g., modulation depth or visibility ($\overline{V}$) of the signal [30].

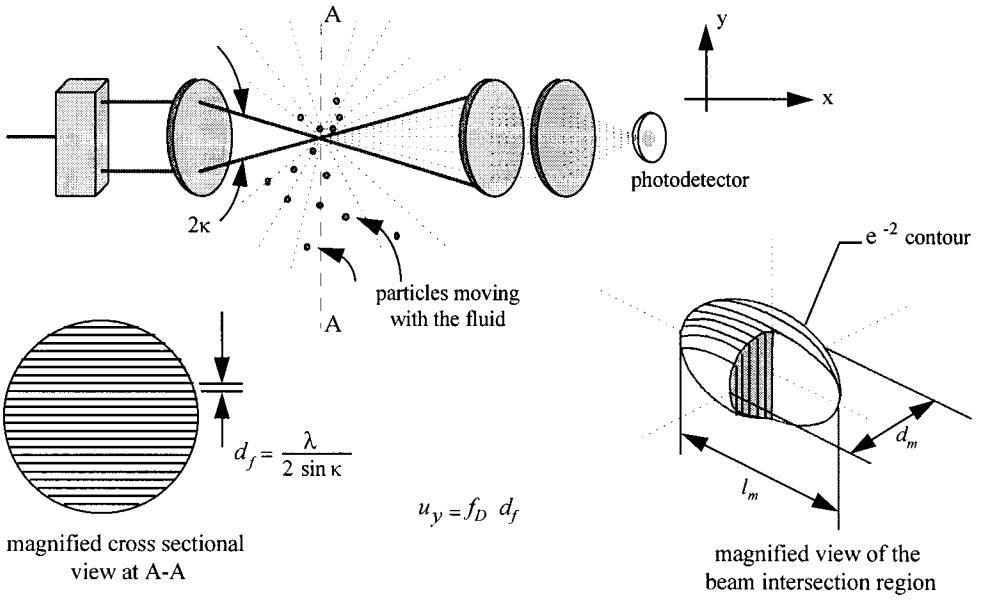

FIGURE 29.25 Details of the beam crossing.

The time taken by the particle to cross the measuring volume is referred to as *transit time*, *residence time*, or *total burst time*, τ_B, and corresponds to the duration of the scattered light signal. The number of cycles (N) in the signal (same as the number of fringes the particle crosses) is given by the product of the transit time (τ_B) and the frequency, f_D, of the signal.

It should also be noted that the fringe spacing (d_f), depends only on the wavelength of the laser light (λ) and the angle (2κ) between the two beams. It can be shown that the effect of the fluid refractive index on these two terms tends to cancel out and, hence, the value of fringe spacing is independent of the fluid medium [31]. The values of λ and κ are known for any dual-beam system and, hence, an actual velocity calibration is not needed. In some cases, an actual velocity calibration using the rim of a precisely controlled rotating wheel has been performed to overcome the errors in measuring accurately the angle between the beams.

The intensity distribution in a laser beam operating in the TEM_{00} mode is Gaussian [32]. Using wave theory and assuming diffraction-limited optics, the effective diameter of the laser beam and the size of the measurement region can be defined. The conventional approach to the definition of laser beam diameter and measuring volume dimensions is based on the locations where the light intensity is $1/e^2$ of the maximum intensity (at the center of the beam). This definition of the dimensions is analogous to that of the boundary layer thickness. The dimensions d_m and l_m of the ellipsoidal measuring volume (Figure 29.25) are based on the $1/e^2$ criterion and are given by:

$$d_m = 4f\lambda / \pi D_{e^{-2}}; \quad l_m = d_m / \tan\kappa; \quad N_{FR} = d_m / d_f \tag{29.69}$$

N_{FR} is the maximum number of fringes in the ellipsoidal measuring region. Note that as the value of $D_{e^{-2}}$ increases, the measuring volume becomes smaller. In flow measurement applications, this relationship is exploited to arrive at the desired size of the measuring volume.

The measuring volume parameters for the following sample situation are wavelength, $\lambda = 514.5$ nm (green line of argon-ion laser), $D_{e^{-2}} = 1.1$ mm, $d = 35$ mm, and $f = 250$ mm. Then, $\kappa = 4°$, $d_m = 149$ μm, and $l_m = 2.13$ mm. The fringe spacing, d_f, is 3.67 μm and the maximum number (N_{FR}) of fringes (number of cycles in a signal burst for a particle going through the center of the measuring volume in the

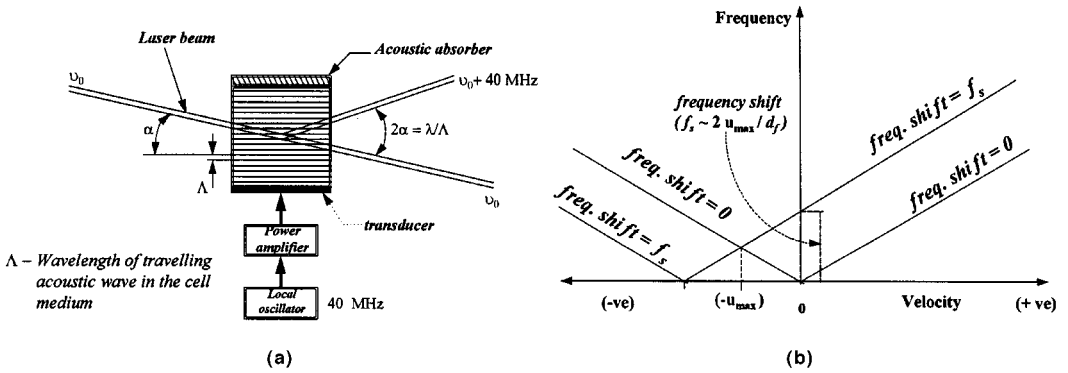

FIGURE 29.26 (*a*) Bragg cell arrangement; (*b*) velocity vs. frequency.

y-direction) in the measuring volume is 40. Consider a particle passing through the center of the measuring region with a velocity (normal to the fringes) of 15 m s^{-1}. This would generate a signal with a frequency of about 4.087 MHz. The transit time of the particle (same as duration of the signal) would be approximately 9.93 μs!

Frequency Shifting

The presence of high turbulence intensity and recirculating or oscillatory flow regions is common in most flow measuring situations. In the fringe model and the Doppler shift (with $f_3 = 0$) descriptions of the dual-beam system, the Doppler signal does not indicate the influence of the sign (positive or negative) of the velocity. Further, a particle passing through the measuring volume parallel to the fringes would not cross any fringes and, hence, not generate a signal having the cyclic pattern resulting in the inability to measure the zero normal (to the fringes) component of velocity. In addition, signal processing hardware used to extract the frequency information often requires the signals to have a minimum number of cycles. This, as well as the ability to measure flow reversals, is achieved by a method of frequency offsetting referred to as *frequency shifting*. Frequency shifting is also used to measure small velocity components perpendicular to the dominant flow direction and to increase the effective velocity measuring range of the signal processors [31].

By introducing a phase or frequency offset (f_s) to one of the two beams in a dual-beam system, the directional ambiguity can be resolved. From the fringe model standpoint, this situation corresponds to a moving (instead of a stationary) fringe system. A stationary particle in the measuring volume will provide a continuous signal at the photodetector output whose frequency is equal to the difference in frequency, f_s, between the two incident beams. In other words, as shown in Figure 29.26(*b*), the linear curve between velocity and frequency is offset along the positive frequency direction by an amount equal to the frequency shift, f_s. Motion of a particle in a direction opposite to fringe movement would provide an increase in signal frequency, while particle motion in the direction of fringe motion would provide a decrease in frequency. To create a signal with an adequate number of cycles even while measuring negative velocities (e.g., flow reversals, recalculating flows), a convenient "rule-of-thumb" approach for frequency shifting is often used. The approach is to select the frequency shift ($f_s \sim 2\ u_{max}/d_f$) to be approximately twice the frequency corresponding to the magnitude of the maximum negative velocity (u_{max}) expected in the flow. This provides approximately equal probability of measurement for all particle trajectories through the measuring volume [33, 34].

Frequency shifting is most commonly achieved by sending the laser beam through a Bragg cell (Figure 29.26(*a*)), driven by an external oscillator [35]. Typically, the propagation of the 40 MHz acoustic wave (created by a 40 MHz drive frequency) inside the cell affects the beam passing through the cell to yield a frequency shift of 40 MHz for that beam. By properly adjusting the angle the cell makes with the incoming beam and blocking off the unwanted beams, up to about 80% of input light intensity is

recovered in the shifted beam. The Bragg cell approach will provide a 40 MHz frequency shift in the photodetector output signal. To improve the measurement resolution of the signal processor, the resulting photodetector signal is often "downmixed" to have a more appropriate frequency shift (based on the rule-of-thumb shift value) for the flow velocities being measured. Frequency shifting using two Bragg cells (one for each beam of a dual-beam system) operating at different frequencies is attractive to systems where the bandwidth of the photodetector is limited. However, the need to readjust the beam crossing with a change in frequency shift has not made this approach (double Bragg cell technique) attractive for applications where frequency shift needs to be varied [31].

More recently, Bragg cells have been used in a multifunctional mode to split the incoming laser beam into two equal intensity beams, with one of them having the 40 MHz frequency shift. This is accomplished by adjusting the Bragg cell angle differently. In addition to Bragg cells, rotating diffraction gratings and other mechanical approaches have been used for frequency shifting. However, limits on rotational speed and other mechanical aspects of these systems make them limited in frequency range [20]. Other frequency shifting techniques have been suggested for use with laser diodes [36, 37]. Because so many flow measurement applications involve recirculating regions and high turbulence intensities, frequency shifting is almost always a part of an LDV system used for flow measurement.

Signal Strength

Understanding the influence of various parameters of an LDV system on the signal-to-noise ratio (SNR) of the photodetector signal provides methods or approaches to enhance signal quality and hence improve the performance of the measuring system. The basic equation for the ratio of signal power to noise power (SNR) of the photodetector signal can be written as [38]:

$$\mathrm{SNR} = A_1 \frac{\eta_q P_0}{\Delta f} \left[\frac{D_a}{r_a} \frac{D_{e^{-2}}}{f} \right]^2 d_p^2 \, \overline{G} \, \overline{V}^2 \tag{29.70}$$

Equation 29.70 shows that higher laser power (P_0) provides better signal quality. The quantum efficiency of the photodetector, η_q depends on the type of photodetector used and is generally fixed. The SNR is inversely proportional to the bandwidth, Δf, of the Doppler signal. The term in brackets relates to the optical parameters of the system; the "*f*-number" of the receiving optics, D_a/r_a, and the transmitting optics, $D_{e^{-2}}/f$. The square dependence of SNR on these parameters makes them the prime choice for improving signal quality and, hence, measurement accuracy. The focal length of the transmitting (f) and receiving (r_a) lenses are generally decided by the size of the flow facility. Using the smallest possible values for these would increase the signal quality. The first ratio (D_a is the diameter of the receiving lens) determines the amount of the scattered light that is collected, and the second ratio determines the diameter of (and hence the light intensity in) the measuring volume. The last three terms are the diameter, d_p, of the scattering center and the two terms (scattering gain $\overline{G}$, visibility $\overline{V}$) relating to properties of the scattered light. These need to be evaluated using the Mie scattering equations [38] or the generalized Lorentz–Mie theory [39].

Measuring Multiple Components of Velocity

A pair of intersecting laser beams is needed to measure (Figure 29.24) one component of velocity. This concept is extended to measure two components of velocity (perpendicular to the optical axis) by having two pairs of beams that have an overlapping intersection region. In this case, the plane of each pair of beams is set to be orthogonal to that of the other. The most common approach to measure two components of velocity is to use a laser source that can generate multiwavelength beams so that the wavelength of one pair of beams is different from the other pair. The Doppler signals corresponding to the two components of velocity are separated by wavelength [31].

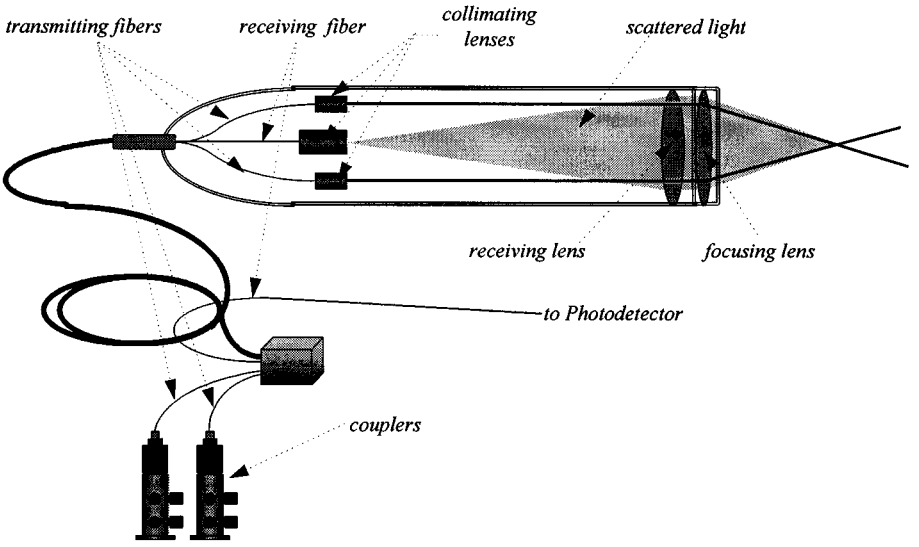

FIGURE 29.27 Schematic arrangement of a fiberoptic system.

Historically, LDV systems were assembled by putting together a variety of optical modules. These modules included beam splitters, color separators, polarization rotators, and scattered light collection systems. The size of such a modular system depended on the number of velocity components to be measured.

The use of optical fibers along with multifunctional optical elements has made the systems more compact, flexible, and easier to make measurements. The laser, optics to generate the necessary number of beams (typically, one pair per component of velocity to be measured), photodetectors, and electronics can be isolated from the measurement location [40]. The fibers carrying the laser beams thus generated are arranged in the probe to achieve the desired beam geometry for measuring the velocity components. Hence, flow field mapping is achieved by moving only the fiber-optic probes, while keeping the rest of the system stationary. To achieve maximum power transmission efficiency and beam quality, special single-mode, polarization-preserving optical fibers along with precision couplers are used. In most cases, these fiber probes also have a receiving system and a separate fiber (multimode) to collect (in back scatter) the scattered light and carry that back to the photodetector system.

A schematic arrangement of a fiber probe system to measure one component of velocity is shown in Figure 29.27. In flow measurement applications, LDV systems using these types of fiber-optic probes have largely replaced the earlier modular systems.

The best way to make three-component of velocity measurements is to use an arrangement using two probes [13]. In this case, the optical axis of the system to measure the third component of velocity (u_x) is perpendicular to that of the two-component system. Unfortunately, access and/or traversing difficulties often make this arrangement impractical or less attractive. In most practical situations, the angle between the two probes is selected to be less than 90°. Such an arrangement using two fiber-optic probes to measure three components of velocity simultaneously is shown in Figure 29.28.

Signal Processing

Nature of the Signal

Every time a particle passes through the measuring region, the scattered light signal level (Figure 29.29) suddenly increases ("burst"). The characteristics of the burst signal are (1) amplitude in the burst not constant, (2) lasts for only a short duration, (3) amplitude varies from burst to burst, (4) presence of noise, (5) high frequency, and (6) random arrival.

FIGURE 29.28 Three-component LDV system with fiber-optic probes.

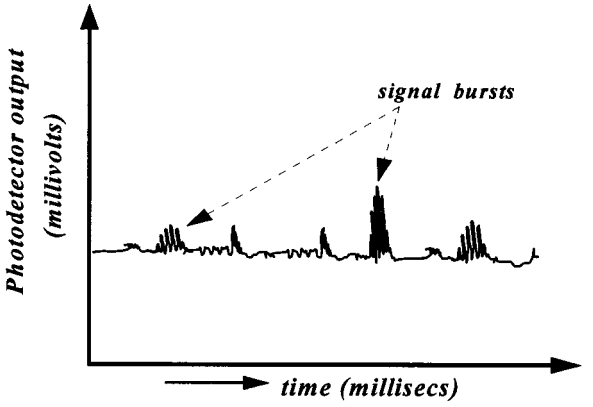

FIGURE 29.29 Time history of the photodetector signal.

The primary task of the signal processor is to extract the frequency information from the burst signal generated by a particle passing through the measuring volume, and provide an analog or digital output proportional to the frequency of the signal. The unique nature of the signals demands the use of a special signal processing system to extract the velocity information.

A variety of techniques has been used for processing Doppler signals. Signal processors have been based on spectrum analysis, frequency tracking, photon correlation, frequency counting, Fourier transform, and autocorrelation principles. The evolution of the signal processing techniques shows the improvement in their ability to handle more difficult measuring situations (generally implies noisier signals), give more accurate measurements, and have higher processing speed.

The traditional instrument to measure signal frequency is a spectrum analyzer. The need to measure individual particle velocities, and to obtain the time history and other properties of the flow, has eliminated the use of "standard" spectrum analyzers [29]. The "tracker" can be thought of as a fixed bandwidth filter that "tracked" the Doppler frequency as the fluid velocity changed. This technique of "tracking flow" worked quite well at modest velocities and where the concentration of scattering centers was high enough to provide an essentially continuous signal. However, too frequently these conditions could not be met in the flows of most interest [29].

When the scattered light level is very low, the photodetector output reveals the presence of the individual photon pulses. By correlating the actual photon pulses from a wide bandwidth photodetector, the photon correlator was designed to work in situations where the attainable signal intensity was very low (low SNR). However, as normally used, it could not provide the velocity of individual particles but only the averaged quantities, such as mean and turbulence intensities.

The "counter" type processor was developed next, and basically measured the time for a certain number (typically, eight) of cycles of the Doppler signal. Although it measured the velocity of individual particles, it depended on the careful setting of amplifier gain and, especially, threshold levels to discriminate between background noise and burst signals. Counters were the processors of choice for many years, and excellent measurements were obtained [42]. However, the reliance on user skill, the difficulty in handling low SNR signals, the possibility of getting erroneous measurements, the inclination to ignore signals from small particles, and the desire to make measurements close to surfaces and in complex flows led to the need for a better signal processor.

Digital Signal Processing

The latest development in signal processing is in the area of digital signal processors. Recent developments in high-speed digital signal processing now permit the use of these techniques to extract the frequency from individual Doppler bursts fast enough to actually follow the flow when the seeding concentration is adequate in a wide range of measurement situations. By digitizing the incoming signal and using the Fourier transform [43] or autocorrelation [44] algorithms, these new digital processors can work with lower SNR signals (than counters), while generally avoiding erroneous data outputs. While instruments using these techniques are certainly not new, standard instruments were not designed to make rapid individual measurements on the noisy, short-duration burst signals with varying amplitudes that are typical of Doppler bursts.

Because the flow velocity and hence the signal frequency varies from one burst to the next, the sampling rate needs to be varied accordingly. And because the signal frequency is not known *a priori*, the ability to optimally sample the signal has been one of the most important challenges in digital signal processing. In one of the digital signal processors, the question of deciding the sample rate is addressed by a burst detector that uses SNR to identify the presence of a signal [44]. In addition, the burst detector provides the duration and an approximate estimate of the frequency of each of the burst signals. This frequency estimate is used to select the output of the sampler (from the many samplers) that had sampled the burst signal at the optimum rate. Besides optimizing the sample rate for each burst, the burst detector information is also used to focus on and process the middle portion of the burst where the SNR is maximum. These optimization schemes, followed by digital signal processing, provide an accurate digital output that is proportional to the signal frequency, and hence the fluid velocity.

Seeding and Other Aspects

The performance of an LDV system can be significantly improved by optimizing the source of the signal, the scattering particle. The first reaction of many experimentalists is to rely on the particles naturally present in the flow. There are a few situations (e.g., LDV systems operating in forward scatter to measure water or liquid flows) where the particles naturally present in the flow are sufficient in number and size to provide good signal quality and hence good measurements. In most flow measurement situations, particles are added to the flow (generally referred to as seeding the flow) to obtain an adequate number of suitable scatterers. Use of a proper particle can result in orders of magnitude increase in signal quality (SNR), and hence can have greater impact on signal quality than the modification of any other component in the LDV system. Ideally, the seed particles should be naturally buoyant in the fluid, provide adequate scattered light intensity, have large enough number concentration, and have uniform properties from particle to particle. While this ideal is difficult to achieve, adequate particle sources and distribution systems have been developed [29, 45–47].

LDV measurements of internal flows such as in channels, pipes and combustion chambers result in the laser beams (as well as the scattered light) going through transparent walls or "windows." In many cases, the window is flat and, hence, the effect of light refraction can be a simple displacement of the measuring region. In the case of internal flows with curved walls, each beam can refract by different amounts and the location of the measuring region needs to be carefully estimated [48]. For internal flows in models with complex geometries, the beam access needs to be carefully selected so that the beams do cross inside. Further, to make measurements close to the wall in an internal flow, the refraction effect of the wall material on the beam path needs to be minimized. One of the approaches is to use a liquid [49] that has the same refractive index as that of the wall material.

Data Analysis

The flow velocity is "sampled" by the particle passing through the measuring volume, and the velocity measurement is obtained only when the Doppler signal, created by the particle, is processed and output as a data point by the signal processor. While averaging the measurements to get, for example, mean velocity would seem reasonable, this method gives the wrong answer. This arises from the fact that the number of particles going through the measuring region per unit time is higher at high velocities than at low velocities. In effect, there is a correlation between the measured quantity (velocity) and the sampling process (particle arrival). Hence, a simple average of the data points will bias the mean value (and other statistical parameters) toward the high-velocity end and is referred to as *velocity bias* [50]. The magnitude of the bias error depends on the magnitude of the velocity variations about the mean. If the variations in velocity are sufficiently small, the error might not be significant.

If the actual data rate is so high that the output data is essentially able to characterize the flow (time history), then the output can be sampled at uniform time increments. This is similar to the procedure normally used for sampling a continuous analog signal using an ADC. This will give the proper value for both the mean and the variance when the data rate is sufficiently high compared to the rates based on the Taylor microscale for the temporal variation of velocity. This is referred to as a high data density situation [29].

In many actual measurement situations, the data rate is not high enough (low data density) to actually characterize the flow. Here, sampling the output of the signal processor at uniform time increments will not work because the probability of getting an updated velocity (new data point) is higher at high velocity than at low velocity (velocity bias). The solution to the velocity bias problem is to weight the individual measurements with a factor inversely proportional to the probability of making the measurement.

$$\overline{U} = \frac{\Sigma u_j \tau_{Bj}}{\Sigma \tau_{Bj}} \tag{29.71}$$

where u_j = Velocity of particle j
τ_{Bj} = Transit time for particle j

Similar procedures can be used to obtain unbiased estimators for variance and other statistical properties of the flow [29]. Modern signal processors provide the residence time and the time between data points along with the velocity data. A comparison of some of the different approaches to do bias correction has been presented by Gould and Loseke [51]. Some of the other types of biases associated with LDV have been summarized by Edwards [52].

A variety of techniques to obtain spectral information of the flow velocity from the random data output of the signal processors have been tried. The goal of all these techniques has been to get accurate and unbiased spectral information to as high a frequency as possible. Direct spectral estimation of the digital output of the processors [53] exhibit the spectrum estimates at high frequency to be less reliable. The "slotting" technique [54, 55] of estimating the autocorrelation of the (random) velocity data followed

by Fourier transform continues to be attractive from a computational standpoint. To obtain reliable spectrum estimates at high frequencies, a variety of methods aimed at interpolation of measured velocity values have been attempted. These are generally referred to as *data* or *signal reconstruction* techniques. A review article [37] emphasizes the need to correct for velocity bias in the spectrum estimates. It also covers some of the recent reconstruction algorithms and points out the difficulties in coming up with a general-purpose approach.

Extension to Particle Sizing

In LDV, the frequency of the scattered light signal provides the velocity of the scatterer. Processing the scattered light to get information about the scatterer other than velocity has always been a topic of great interest in flow and particle diagnostics. One of the most promising developments is the extension of the LDV technique to measure the surface curvature and, hence, the diameter of a spherical scatterer [22]. This approach (limited to spherical particles) uses the phase information of the scattered light signal to extract the size information. To obtain a unique and, preferably, monotonic relation between phase of the signal and the size of the particle, the orientation and the geometry (aperture) of the scattered light collection system needs to be carefully chosen. In the following, unless otherwise mentioned, the particles are assumed to be spherical.

The light scattered by a particle, generally, contains contributions from the different scattering mechanisms — reflection, refraction, diffraction, and internal reflection(s). It can be shown that, by selecting the position of the scattered light collection set-up, contributions from one scattering mechanism can be made dominant over the others. The aim in phase Doppler measurements is to have the orientation of the receiver system such that the scattered light collected is from one dominant scattering mechanism.

The popularity of the technique is evidenced by its widespread use for measuring particle diameter and velocity in a large number of applications, especially in the field of liquid sprays [56]. The technique has also been used in diagnosing flow fields associated with combustion, cavitation, manufacturing processes, and other two-phase flows.

Phase Doppler System: Principle

The phase Doppler approach, outlined as an extension to an LDV system, was first proposed by Durst and Zare [57] to measure velocity and size of spherical particles. The first practical phase Doppler systems using a single receiver were proposed by Bachalo and Houser [22].

A schematic arrangement of a phase Doppler system is shown in Figure 29.30(*a*). This shows a receiver system arrangement that collects, separates, and focuses the scattered light onto multiple photodetectors. In general, the receiving system aperture is divided into three parts and the scattered light collected through these are focused into three separate photodetectors. For simplicity, in Figure 29.30(*a*), the output of two detectors are shown. The different spatial locations of the detectors (receiving apertures) results in the signals received by each detector having a slightly different phase. In general, the difference in phase between the signals from the detectors is used to obtain the particle diameter whereas the signal frequency provides the velocity of the particle.

Fringe Model Explanation

The fringe model provides an easy and straightforward approach to arrive at the expressions for Doppler frequency and phase shift created by a particle going through the measuring volume. As the particle moves through the fringes in the measuring volume, it scatters the fringe pattern (Figure 29.30(*b*)). The phase shift in the signals can be examined by looking at the scattered fringe pattern. If the particle acts like a spherical mirror (dominant reflection) or a spherical lens (dominant refraction), it projects fringes from the measuring volume into space all around as diverging bands of bright and dark light, known as *scattered fringes*. Scattered fringes as seen on a screen placed in front of the receivers are shown in Figure 29.30(*b*). The spacing between the scattered fringes at the plane of the receiver is s_f. The receiver system shown in Figure 29.30(*b*) shows two apertures. The distance between (separation) the centroids

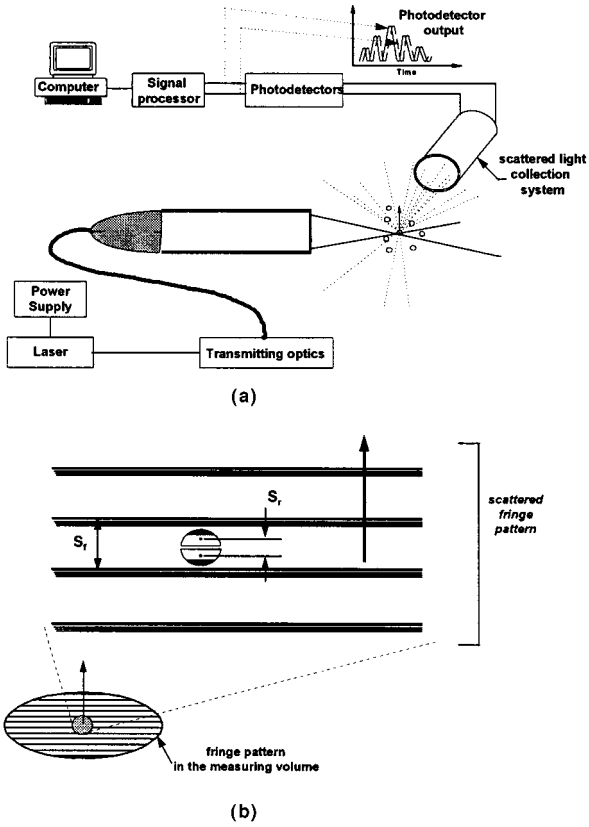

FIGURE 29.30 (*a*) Phase/Doppler system: schematic. (*b*) phase/Doppler System: fringe model.

of the two receiving apertures is s_r. Scattered fringes move across the receivers as the particle moves in the measuring volume, generating temporally fluctuating signals. The two photodetector output signals are shifted in phase by s_r/s_f times 360° [31]. Large particles create a scattered fringe pattern with a smaller fringe spacing (compared to that for small particles), i.e., particle diameter is inversely proportional to s_f, while s_f is inversely proportional to phase difference. Thus, the fringe model shows the particle diameter to be directly proportional to the phase difference. It can also be seen that the sensitivity (degrees of phase difference per micrometer) of the phase Doppler system can be increased by increasing the separation (s_r) between the detectors.

The phase Doppler system shown above measures the phase difference between two detectors in the receiver system to obtain particle diameter. This brings in the limitation that the maximum value of phase that could be measured is 2π. A three-detector arrangement in the receiver system is used to overcome this 2π ambiguity. Figure 29.31 shows the three-detector (aperture) arrangement. Scattered light collected through apertures 1, 2, and 3 are focused into detectors 1, 2, and 3. Φ_{13} is the phase difference between the detectors 1 and 3 and provides the higher phase sensitivity because of their greater separation compared to detectors 1 and 2. As Φ_{13} exceeds 2π, the value of Φ_{12} is below 360° and is used to keep track of Φ_{13}. It should be noted that the simplified approach in terms of geometrical scattering provides a linear relationship between the phase difference and diameter of the particle.

It has been pointed out that significant errors in measured size can occur due to trajectory-dependent scattering [58]. These errors could be minimized by choosing the appropriate optical configuration of the phase Doppler system [59]. An intensity-based validation technique has also been proposed to reduce the errors [60].

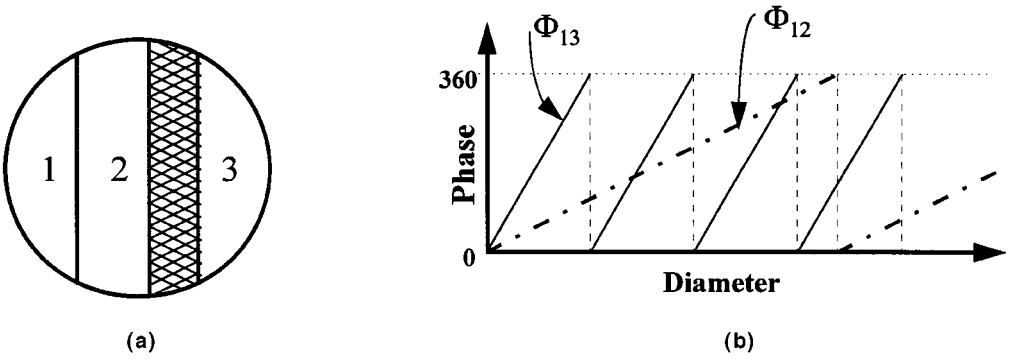

FIGURE 29.31 (*a*) Three-detector configuration; (*b*) phase–diameter relationship.

To explore the fundamental physical limits on applicability of the Phase Doppler technique, a rigorous model based on the electromagnetic theory of light has been developed. Computational results based on Mie scattering and comparison with and limitations of the geometric scattering approach have also been outlined by Naqwi and Durst [61]. These provided a systematic approach to develop innovative solutions to particle sizing problems. A new approach (PLANAR arrangement) to achieve high measurement resolution provided the ability to extend the measurement range to submicrometer particles. The Adaptive Phase Doppler Velocimeter (APV) system [59] that incorporates this layout uses a scattered light collection system that employs independent receivers. In the APV system, the separation between the detectors is selectable and is not dependent on the numerical aperture of the receiving system. Such a system was used for measuring submicrometer droplets in an electrospray [62]. By integrating a phase Doppler velocimeter system with a *rainbow refractometer* system, the velocity, size, and the refractive index of a droplet could be determined [63].

The velocity and diameter information is obtained by processing the photodetector output signals. The frequency of the photodetector output signal provides the velocity information. In general, the signal processing system for velocity measurements is expanded to measure the phase difference between two photodetector signals. The digital signal processing approaches described earlier have been complimented by the addition of accurate phase measurement techniques [64, 65].

Although the phase Doppler technique is limited to spherical particles, there has always been an interest in extending the technique to nonspherical particles. In the past, symmetry checks [66] and other similar techniques have been used to check on the sphericity of particles. An equivalent sphere approach has been used to describe these nonspherical particles. Sizing irregular particles is a more complex problem because the local radius of curvature concept is not meaningful in these cases. An innovative stochastic modeling approach has been used to study irregular particles using a phase Doppler system [67].

Conclusion

LDV has become the preferred technique for measuring flow velocity in a wide range of applications. The ability to measure noninvasively the velocity, without calibration, of any transparent flowing fluid has made it attractive for measuring almost any type of flow. Velocity measurement of moving surfaces by LDV is used to monitor and control industrial processes. Use of laser diodes, fiber optics, and advances in signal processing and data analysis are reducing both the cost and complexity of measuring systems. The extension of LDV to the phase Doppler technique provides an attractive, noncontact method for measuring size and velocity of spherical particles. Recent developments in the phase Doppler technique have generated a method to size submicrometer particles as well. These ideas have been extended to examine irregular particles also.

Acknowledgments

The input and comments from Dr. L. M. Fingerson and Dr. A. Naqwi of TSI Inc. have been extremely valuable in the preparation of this chapter section. The author is sincerely grateful to them for the help.

References

1. D. Niccum, A new tool for fiber spinning process control and diagnostics, *Int. Fiber J.,* 10(1), 48-57, 1995.
2. R. Schodl, On the extension of the range of applicability of LDA by means of a the laser-dual-focus (L-2-F) technique, *The Accuracy of Flow Measurements by Laser Doppler Methods*, Skovulunde, Denmark: Dantec Measurement Technology, 1976, 480-489.
3. R. J. Adrian, Particle imaging techniques for experimental fluid mechanics, *Annu. Rev. Fluid Mech.,* 23, 261-304, 1991.
4. I. Grant, *Selected Papers in Particle Image Velocimetry,* SPIE Milestone Series, MS 99, Bellingham, WA: SPIE Optical Engineering Press, 1994.
5. R. J. Adrian, *Bibliography of Particle Velocimetry Using Imaging Methods: 1917–1995,* TAM Report, University of Illinois Urbana-Champaign, Produced and distributed in cooperation with TSI Inc., March 1996. (Also available in electronic format.)
6. W. T. Lai, Particle image velocimetry: a new approach to experimental fluid research, in *Three Dimensional Velocity and Vorticity Measuring and Image Analysis Techniques*, Th. Dracos (ed.), Boston: Kluwer Academic, 1996, 61-92.
7. M. M. Koochesfahani, R. K. Cohn, C. P. Gendrich, and D. G. Nocera, Molecular tagging diagnostics for the study of kinematics and mixing in liquid phase flows, *8th Int. Symp. Appl. Laser Techniques Fluid Mechanics,* Lisbon, 1996.
8. H. Komine, S. J. Brosnan, A. B. Litton, and E. A. Stappaerts, Real time Doppler global velocimetry, *AIAA 29th Aerospace Sciences Meeting,* Paper No. AIAA-91-0337, January 1991.
9. R. L. McKenzie, Measurement capabilities of planar Doppler velocimetry using pulsed lasers, *Appl. Opt.,* 35, 948-964, 1996.
10. C. Berner, Supersonic base flow investigation over axisymmetric bodies, *Proc. 5th Inc. Conf. Laser Anemometry and Applications,* Netherlands, SPIE, 2052, 1993.
11. K. Jaffri, H. G. Hascher, M. Novak, K. Lee, H. Schock, M. Bonne, and P. Keller, Tumble and Swirl Quantification within a Four-valve SI Engine Cylinder Based on 3D LDV Measurements, SAE Paper No. 970792, Feb. 1997.
12. G. G. Podboy and M. J. Krupar, Laser Velocimeter Measurements of the Flow Field Generated by a Forward-Swept Propfan During Flutter, NASA Technical Memorandum 106195, 1993.
13. Y. O. Han, J. G. Leishman, and A. J. Coyne, Measurements of the velocity and turbulence structure of a rotor tip vortex, *AIAA J.,* 35, 477-485, 1997.
14. T. Mathur and J. C. Dutton, Velocity and turbulence measurements in a supersonic base flow with mass bleed, *AIAA J.,* 34, 1153-1159, 1996.
15. E. J. Johnson, P. V. Hyer, P. W. Culotta, and I. O. Clark, Laser velocimetry in nonisothermal CVD systems, *Proc. 4th Int. Conf. Laser Anemometry,* Cleveland, OH, August 1991.
16. R. W. Dibble, V. Hartmann, R. W. Schefer, and W. Kollmann, Conditional sampling of velocity and scalars in turbulent flames using simultaneous LDV-Raman scattering, *Exp. Fluids,* 5, 103-113, 1987.
17. D. V. Srikantiah and W. W. Wilson, Detection of a pulsed flow in an MHD environment by laser velocimetry, *Exp. Fluids,* 6, 500-503, 1988.
18. P. O. Witze, Velocity measurements in end-gas region during homogeneous-charge combustion in a spark ignition engine, *Laser Techniques and Applications in Fluid Mechanics*, Adrian, et al. (eds.), Lisbon: Ladoan, 1992, 518-534.

19. G. L. Morrison, M. C. Johnson, R. E. DeOtte, H. D. Thames, and B. J. Wiedner, An experimental technique for performing 3D LDA measurements inside whirling annular seals, *Flow Meas. Instrum.,* 5, 43-49, 1994.
20. F. Durst, A. Melling, and J. H. Whitelaw, *Principles and Practice of Laser Doppler Anemometry,* 2nd ed., New York: Academic Press, 1981.
21. R. J. Adrian (ed.), *Selected Papers on Laser Doppler Velocimetry*, SPIE Milestone Series, MS 78, Bellingham, WA: SPIE Optical Engineering Press, 1993.
22. W. D. Bachalo and M. J. Houser, Phase Doppler spray analyzer for simultaneous measurements of drop size and velocity distributions, *Opt. Eng.,* 23, 583-590, 1984.
23. Y. Yeh and H. Z. Cummins, Localized fluid flow measurements with an He-Ne laser spectrometer, *Appl. Phys. Lett.,* 4, 176-178, 1964.
24. C. M. Penney, Differential Doppler velocity measurements, *IEEE J. Quantum Electron.,* QE-5, 318, 1969.
25. L. M. Fingerson and P. Freymuth, Thermal anemometers, in *Fluid Mechanics Measurements,* R. J. Goldstein (ed.), New York: Hemisphere, 1983, 99-154.
26. G. Smeets and A. George, Michelson spectrometer for instantaneous Doppler velocity measurements, *J. Phys. E: Sci. Instrum.,* 14, 838-845, 1981.
27. D. Brayton, Small particle signal characteristics of a dual scatter laser velocimeter, *J. Appl. Opt.,* 13, 2346-2351, 1974.
28. F. Durst and W. H. Stevenson, Moiré patterns to visually model laser Doppler signals, *The Accuracy of Flow Measurements by Laser Doppler Methods*, Skovulunde, Denmark: Dantec Measurement Technology, 1976, 183-205.
29. R. J. Adrian, Laser Velocimetry, in *Fluid Mechanics Measurements,* R. J. Goldstein (ed.), New York: Hemisphere, 1983, 155-240.
30. R. J. Adrian and K. L. Orloff, Laser anemometer signal: visibility characteristics and application to particle sizing, *Appl. Opt.,* 16, 677-684, 1977.
31. L. M. Fingerson, R. J. Adrian, R. K. Menon, S. L. Kaufman, and A. Naqwi, Data Analysis, Laser Doppler Velocimetry and Particle Image Velocimetry, TSI Short Course Text, TSI Inc., St. Paul, MN, 1993.
32. H. Kogelnik and T. Li, Laser beams and resonators, *Appl. Opt.,* 5, 1550-1567, 1966.
33. M. C. Whiffen, Polar response of an LV measurement volume, *Minnesota Symp. Laser Anemometry,* University of Minnesota, 1975.
34. C. Tropea, A practical aid for choosing the shift frequency in LDA, *Exp. Fluids,* 4, 79-80, 1986.
35. M. K. Mazumder, Laser Doppler velocity measurement without directional ambiguity by using frequency shifted incident beams, *Appl. Phys. Lett.,* 16, 462-464,1970.
36. H. Muller, V. Tobben, V. Arndt, V. Strunck, H. Wang, R. Kramer, and D. Dopheide, New frequency shift techniques in laser anemometry using tunable semiconductor lasers and solid state lasers, *Proc. 2nd Int. Conf. Fluid Dynamic Measurement Applications,* Beijing, Oct. 1994, 3-19.
37. E. Muller, H. Nobach, and C. Tropea, LDA signal reconstruction: application to moment and spectral estimation, *Proc. 7th Int. Symp. Applications Laser Techniques Fluid Mechanics,* Lisbon, 1994b.
38. R. J. Adrian and W. L. Early, Evaluation of laser Doppler velocimeter performance using Mie scattering theory, *Proc. Minnesota Symp. Laser Anemometry,* University of Minnesota, 1975, 429-454.
39. G. Grehan, G. Gouesbet, A. Naqwi, and F. Durst, Trajectory ambiguities in phase Doppler systems: study of a new forward and a near-backward geometry, *Part. Part. Syst. Charact.,* 11, 133-144, 1994.
40. D. J. Fry, Model submarine wake survey using internal LDV probes, *Proc. ASME Fluids Engineering Meeting,* T. T. Huang, J. Turner, M. Kawahashi, and M. V. Otugen (eds.), FED- Vol. 229, August 1995, 159-170.
41. P. A. Chevrin, H. L. Petrie, and S. Deutsch, Accuracy of a three-component laser Doppler velocimeter system using a single lens approach, *J. Fluids Eng.,* 115, 142-147, 1993.

42. R. I. Karlsson and T. G. Johansson, LDV measurements of higher order moments of velocity fluctuations in a turbulent boundary layer, in *Laser Anemometry in Fluid Mechanics III*, Ladoan-Instituto Superior Technico, 1096 Lisbon Codex, Portugal, 1988, 273-289.
43. K. M. Ibrahim, G. D. Werthimer, and W. D. Bachalo, Signal processing considerations for laser Doppler and phase Doppler applications, *Proc. 5th Int. Symp. Applications Laser Techniques Fluid Mechanics,* Lisbon, 1990.
44. L. Jenson, LDV digital signal processor based on Autocorrelation, *Proc. 6th Int. Symp. Applications Laser Techniques Fluid Mechanics,* Lisbon, 1992.
45. W. W. Hunter and C. E. Nichols (compilers), Wind Tunnel Seeding Systems for Laser Velocimeters, NASA Conference Publication 2393, 1985.
46. A. Melling, Seeding gas flows for laser anemometry, AGARD CP-339, 1986, 8-1–8-11.
47. R. K. Menon and W. T. Lai, Key considerations in the selection of seed particles for LDV measurements, *Proc. 4th Int. Conf. Laser Anemometry,* Cleveland, OH, August 1991.
48. M. L. Lowe and P. H. Kutt, Refraction through cylindrical tubes, *Exp. Fluids,* 13, 315-320, 1992.
49. R. Budwig, Refractive index matching methods for liquid flow investigations, *Exp. Fluids,* 17, 350-355, 1994.
50. D. K. McLaughlin and W. G. Tiederman, Biasing correction for individual realization of laser anemometer measurements in turbulent flows, *Phys. Fluids,* 16, 2082-2088, 1973.
51. R. D. Gould and K. W. Loseke, A comparison of four velocity bias correction techniques in laser Doppler velocimetry, *J. Fluids Eng.,* 115, 508–514, 1993.
52. R. V. Edwards (ed.), Report on the special panel on statistical particle bias problems in laser anemometry, *J. Fluids Eng.,* 109, 89-93, 1987.
53. J. B. Roberts, J. Downie, and M. Gaster, Spectral analysis of signals from a laser Doppler anemometer operating in the burst mode, *J. Physics, E: Sci. Instrum.,* 13, 977-981, 1980.
54. W. T. Mayo, Spectrum measurements with laser velocimeters, *Proc. Dynamic Flow Conf. Dynamic Measurements in Unsteady Flows,* DISA Electronik A/S, Denmark, 1978, 851-868.
55. H. L. Petrie, Reduction of noise effects on power spectrum estimates using the discretized lag product method, *ASME Fluids Engineering Meeting,* FED-229, 139-144, 1995.
56. W. D. Bachalo, A. Brena de la Rosa, and S. V. Sankar, Diagnostics for fuel spray characterization, *Combustion Measurements*, N. Chigier (ed.), New York: Hemisphere, 1991, chap. 7.
57. F. Durst and M. Zare, Laser Doppler measurements in two-phase flows, *The Accuracy of Flow Measurements by Laser Doppler Methods*, Skovulunde, Denmark: Dantec Measurement Technology, 1976, 480-489.
58. M. Saffman, The use of polarized light for optical particle sizing, *Laser Anemometry in Fluid Mechanics III*, Adrian, et al. (eds.), Lisbon: Ladoan, 1988, 387-398.
59. A. Naqwi, Innovative phase Doppler systems and their applications, *Part. Part. Syst. Charact.,* 11, 7-21, 1994.
60. S. V. Sankar, D. A. Robart, and W. D. Bachalo, An adaptive intensity validation technique for minimizing trajectory dependent scattering errors in phase Doppler interferometry, *Proc. 4th Int. Congr. Optical Particle Sizing,* Nuremberg, Germany, March 1995.
61. A. Naqwi and F. Durst, Light scattering applied to LDA and PDA measurements. 2. Computational results and their discussion, *Part. Part. Syst. Charact.,* 9, 66-80, 1992.
62. A. Naqwi, *In-situ* measurement of submicron droplets in electrosprays using a planar phase Doppler system, *J. Aerosol Sci.,* 25, 1201-1211, 1994.
63. S. V. Sankar, D. H. Buermann, D. A. Robart, and W. D. Bachalo, An advanced rainbow signal processor for improved accuracy of droplet temperature measurements in spray flames, *Proc. 8th Int. Symp. Applications Laser Techniques Fluid Mechanics,* Lisbon, 1996.
64. J. Evenstad, A. Naqwi, and R. Menon, A device for phase shift measurement in an advanced phase Doppler velocimeter, *Proc. 8th Int. Symp. Applications Laser Techniques Fluid Mechanics,* Lisbon, 1996.

65. K. M. Ibrahim and W. D. Bachalo, A novel architecture for real-time phase measurement, *Proc. 8th Int. Symp. Applications of Laser Techniques to Fluid Mechanics,* Lisbon, 1996.
66. M. Saffman, P. Buchave, and H. Tanger, Simultaneous measurement of size, concentration and velocity of spherical particles by a laser Doppler method, in *Laser Anemometry in Fluid Mechanics II*, R. J. Adrian, et al. (eds.), Lisbon: Ladoan, 1986, 85-104.
67. A. Naqwi, Sizing of irregular particles using a phase Doppler system, *Proc. ASME Heat Transfer and Fluid Engineering Divisions,* FED-Vol. 233, 1995.

Further Information

C. A. Greated and T. S. Durrani, *Laser Systems and Flow Measurement*, New York: Plenum, 1977.

L. E. Drain, *The Laser Doppler Technique*, New York: John Wiley & Sons, 1980.

Proc. Int. Symp. (1 to 8) *on Applications of Laser Techniques to Fluid Mechanics,* Lisbon, Portugal, 1982, 1984, 1986, 1988, 1990, 1992, 1994, 1996.

P. Buchave, W. K. George, and J. L. Lumley, The measurement of turbulence with the laser Doppler anemometer, *Annu. Rev. Fluid Mech.*, 11, 443-504, 1979.

Proc. 5th Int. Conf. Laser Anemometry and Applications, Netherlands, SPIE, Vol. 2052, 1993.

Proc. ASME Fluids Engineering Meeting, T. T. Huang, J. Turner, M. Kawahashi, and M. V. Otugen, eds., FED- Vol. 229, August 1995.

L. H. Benedict and R. D. Gould, Experiences using the Kalman reconstruction for enhanced power spectrum estimates, *Proc. ASME Fluids Engineering Meeting,* T. T. Huang, J. Turner, M. Kawahashi, and M. V. Otugen (eds.), FED 229, 1-8, 1995.

D. Dopheide, M. Faber, G. Reim, and G. Taux, Laser and avalanche diodes for velocity measurement by laser Doppler anemometry, *Exp. Fluids,* 6, 289-297, 1988.

F. Durst, R. Muller, and A. Naqwi, Measurement accuracy of semiconductor LDA systems, *Exp. Fluids,* 10, 125-137, 1990.

A. Naqwi and F. Durst, Light scattering applied to LDA and PDA measurements. 1. Theory and numerical treatments, *Particle and Particle System Characterization,* 8, 245-258, 1991.